Soil & Tillage Research 259 (2026) 107069

Contents lists available at ScienceDirect

Soil & Tillage Research

journal homepage: www.elsevier.com/locate/still

Evaluating the effects of earthworm tip geometry on burrowing forces using cone penetration analogues and GPU-based discrete element method (DEM) simulations

Kang Li [c,1], Dániel Nagy [b,1], Thomas Keller [d,e], Kornél Tamás [a,*]

[a] Department of Machine and Product Design, Faculty of Mechanical Engineering, Budapest University of Technology and Economics, Műegyetem rkp. 3., H-1111 Budapest, Hungary
[b] Department of Hydrodynamic Systems, Faculty of Mechanical Engineering, Budapest University of Technology and Economics, Műegyetem rkp. 3., H-1111 Budapest, Hungary
[c] Experimental Zoology Group, Department of Animal Sciences, Wageningen University & Research, De Elst 1, 6708 WD Wageningen, The Netherlands
[d] Department of Soil and Environment, Swedish University of Agricultural Sciences, Box 7014, 75007 Uppsala, Sweden
[e] Department of Agroecology and Environment, Agroscope, Reckenholzstrasse 191, 8046 Zürich, Switzerland

ARTICLE INFO

Keywords:
Earthworm
Mucus
Direct shear box test
Soil simulation
DEM
GPU

ABSTRACT

Earthworms play an essential role in maintaining and restoring soil structure through burrowing. Although the importance of earthworms is well recognized, knowledge on penetration forces and energy requirements of burrowing remain limited. To investigate these mechanisms, we preformed measurements and simulations of cone penetration analogues, with cones that had a center hole to mimic soil ingestion by earthworms. Measurements were carried out to analyze soil displacement patterns for various cone characteristics, while discrete element method (DEM) simulations accelerated by graphical processor units (GPUs) were performed to quantify penetration forces and calculate energy requirements for burrowing. The influence of cone half-angle, the center hole diameter that mimic the mouth opening of an earthworm, and lubrication representing earthworm mucus are explored. The main findings show that more pointed cones reduce penetration force and compaction in the axial direction but limit soil ingestion, while blunter cones increase ingestion at the cost of higher penetration energy. Results indicate that cone half-angles of 25°–30° (given a 2 mm center hole) maximize earthworm burrowing efficiency in the investigated silt loam soil, as in that case available energy from soil ingestion is five-fold the energy requirement of burrowing. Lubrication had little effect in a low organic content silt loam soil while it slightly reduced the required penetration force in a high organic content silt loam soil. Overall, the combination of experiments and DEM simulations offer a mechanistic understanding of soil ingestion of earthworms that was not previously available.

1. Introduction

Earthworms inhabit the vadose zone (unsaturated region above the water table), where their activity has been shown to enhance plant biomass under a range of soil types and moisture conditions (Mao et al., 2024). Earthworm activity is needed for soil structure maintenance as earthworms contribute to various soil functions (Vidal et al., 2023). Their burrowing improves soil aeration and water infiltration, accelerating the recovery from compaction (Uteau et al., 2022; Zhang et al., 2023).

Earthworms burrow through soil using two primary mechanisms: cavity expansion and soil ingestion. Earthworms are able to ingest soil by generating hydrostatic pressure through coordinated muscle contractions of the pharynx, which functions as a suction pump, and in some cases by everting the pharynx to fill it with soil before retraction (Edwards et al., 1996). Previous studies have modeled earthworm burrowing primarily through cavity expansion mechanisms, combining elasto-viscoplastic soil constitutive laws with detailed kinematic descriptions of earthworm motion (Ruiz et al., 2017; Ruiz, 2018). During burrowing, mucus secreted by earthworms helps reduce penetration resistance. Earthworm mucus maintains body surface moisture and is secreted through mucus glands, dorsal pores (coelomic fluid),

* Corresponding author.
E-mail addresses: kang.li.wur.nl@gmail.com (K. Li), dnagy@hds.bme.hu (D. Nagy), thomas.keller@agroscope.admin.ch (T. Keller), tamas.kornel@gt3.bme.hu (K. Tamás).
[1] Kang Li and Dániel Nagy are equal contributors to this work and designated as co-first authors.

https://doi.org/10.1016/j.still.2026.107069
Received 14 October 2025; Received in revised form 19 December 2025; Accepted 10 January 2026

nephridial excretions, and uptake of ground moisture (Gajalakshmi and Abbasi, 2004). Rheological studies have shown that earthworm mucus is non-Newtonian as it exhibits shear thickening behavior at low shear rates and shear-thinning behavior at higher shear rates (Zhang et al., 2016).

The cone penetration test (CPT) has been employed as an analogue for earthworm burrowing (Ruiz et al., 2016) and root penetration (Sinnett et al., 2008; Mishra et al., 2018). Low-speed CPT (200 μm/s) has been applied to study earthworm burrowing at different cone angles (Ruiz et al., 2017), and even to develop earthworm-inspired cones (Cortes and John, 2018). Previous studies have evaluated energy consumption during burrowing by integrating penetration resistance over depth (Ruiz et al., 2017), based on cast production (Arrázola-Vásquez et al., 2022), and by measuring the heat dissipation (Arrazola-Vasquez et al., 2024). However, neither the effect of soil ingestion during burrowing nor the effect of lubrication was considered in previous studies.

To further understand the effect of earthworm burrowing in soil, we reproduce measurements via a GPU-based discrete element method (DEM), and analyze the flow of soil into a cone with a center hole mimicking an earthworm mouth, the associated energy intake, and the resulting particle density distribution around the burrow. DEM allows for the modeling of soil heterogeneity and enables tracking of individual particle displacements in the CPT (Jiang et al., 2014; Cui et al., 2023). Recent advances in GPU-accelerated DEM simulations make it possible to model large particle systems efficiently (Dong et al., 2022; Guo et al., 2023; Nagy et al., 2024), and thus to examine soil particle flow around CPT cones at a finer scale.

For understanding earthworm burrowing behavior, the full energy balance is a critical but still underexplored aspect. While previous studies have estimated the energetic cost of burrowing (Ruiz et al., 2017), they did not account for the energy intake associated with soil ingestion. Soil ingestion can be a key burrowing mechanism for earthworms, particularly under compacted soil conditions. As noted by Arrázola-Vásquez et al. (2022), when soil resistance is high, earthworms increasingly rely on ingestion rather than pure cavity expansion to advance through the soil. From Curry and Schmidt (2007) and Bolton and Phillipson (1976) it is known that geophagous earthworms adopt a feeding strategy based on consuming large volumes of low-quality soil material. In this context, burrowing and feeding are intrinsically coupled processes, with earthworms effectively "eating their way" through the soil. Consequently, accurately representing ingestion mechanics is essential for understanding burrowing efficiency and soil–organism interactions. Considering both the energy required for burrowing (output energy) and the energy gained through soil ingestion (input energy) enables a more comprehensive assessment of the efficiency of earthworm burrowing mechanisms. Additionally, the role of earthworm mucus in facilitating burrowing has not been previously investigated, even though mucus may reduce friction at the burrow wall, influence soil aggregation and adhesion, and potentially lower the energetic cost of penetration (Zhang et al., 2016). Although DEM simulations offer a promising framework to investigate soil ingestion and flow, previous CPT studies typically employed particles that are large relative to the cone dimensions (Ciantia et al., 2016; Khosravi et al., 2020; Chen et al., 2022), limiting their ability to resolve ingestion processes accurately. Consequently, using a larger number of smaller particles is essential when ingested soil volume is of interest, which in turn necessitates efficient parallelization of DEM simulations, for example through GPU acceleration.

Motivated by the above-mentioned knowledge gaps, this study aims to contribute new insights into the mechanisms and energetic efficiency of earthworm burrowing in silt loam soil with varying organic matter content, by using cone penetration analogues. To extend on previous CPT-based studies, cones with center holes are used to mimic the soil ingestion. The first objective of this study is to calibrate micromechanical DEM parameters for two soils with small particles using direct shear box (DSB) tests and a GPU-accelerated DEM solver. Proper calibration for organic matter rich soils required the extension of the Hertz–Mindlin contact model with liquid-bridge and adhesion forces. The second objective is to systematically investigate cone penetration parameters, including cone half-angle (representing earthworm tip shape), central hole diameter (representing earthworm mouth), and lubrication (representing earthworm mucus), and to evaluate how these traits influence penetration forces. The third objective is to quantify soil ingestion and displacement during macropore formation, by combining CPT measurements and DEM simulations to estimate the energy available from soil ingestion, and assess the resulting full energy balance of the burrowing process (i.e., energy use for burrowing in relation to energy content of ingested soil).

Table 1
Identification of the silt loam soils selected for the study.

Soil type	Clay content [m%]	Silt content [m%]	Sand content [m%]	Organic matter [m%]
Low organic silt loam	21.3	59.7	19.0	3.0
High organic silt loam	21.1	59.9	19.0	5.7

2. Materials and methods

2.1. Soils

To explore the soil textures relevant to earthworm burrowing mechanisms, two silt loam soils were selected: one with a lower organic matter content and one with a higher organic matter content. The selected soils were dried, sieved, and rewetted before use. The exact parameters of the soils are given in Table 1. The particle size distribution was obtained by sieving following the ISO 17892-4:2016 standard, while the organic matter content was determined using ignition loss tests following the MSZ 15296:1999 standard. Each soil type was prepared in a compacted condition with a bulk density of 1.5 g/cm^3 and a gravimetric water content of 25%, mimicking unsaturated field conditions that earthworms typically encounter. This bulk density is consistent with previous CPT studies on earthworm burrowing and reflects conditions under which earthworms tend to rely more on soil ingestion (Ruiz et al., 2017; Ducasse et al., 2021; Arrázola-Vásquez et al., 2022), while the selected water content is suitable for earthworms and maintains burrow structure under conditions preferred by some earthworm species (Ruiz et al., 2017; Edwards et al., 1996).

For the direct shear box (DSB) test and the cone penetration test (CPT), all soil samples were first sieved through a mesh with 100 holes per linear inch (0.149 mm). The sieved soils were then dried in an oven at 105 °C for over 24 hours to remove residual moisture, as recommended by the ASTM D2216-19 standard (ASTM, 2019). After drying, the soil was rewetted to a gravimetric water content of 25% using distilled water and thoroughly mixed by hand. To maintain uniform moisture during storage, the samples were kept in a sealed desiccator with water at the bottom (Soil Survey Staff, 2014).

For the CPT, a fixed mass of moist soil was filled into an aluminum ring (55 mm diameter, 40 mm height) in layers. Each layer was lightly scratched before adding the next layer to ensure homogeneity. The soil was compacted and leveled using a hand tamper. The preparation was based on the ASTM D1883-21 standard (ASTM, 2021). For the DSB test, the same procedure was followed, except the soil was packed into a square metal box (60 mm × 60 mm × 20 mm) suitable for the shear box apparatus.

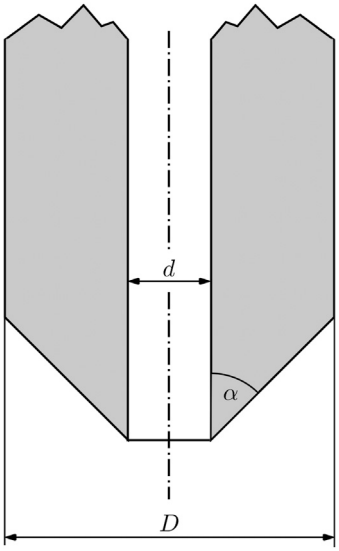

Fig. 1. Geometry of the cone tips, where D is the cone diameter, d is the cone center hole diameter and α is the cone half-angle.

2.2. Direct shear box test

Proper calibration of micromechanical parameters is essential for accurate DEM simulations (Coetzee, 2017). The micromechanical parameters describe the interactions between particles and the properties of particles, and include the parameters such as density, Young's modulus, Poisson's ratio, friction coefficient and coefficient of restitution of the particles. While direct measurement of micromechanical properties is often impractical or impossible, parameter sets can be inferred from macroscopic behavior of the granular medium (Keppler et al., 2016). For more precise calibration and validation, dedicated tests such as the direct shear box (DSB) test are recommended (Bahrami et al., 2020). The standard DSB test has been found successful in determining parameters for DEM simulations of cone penetration (Keppler et al., 2016); thus, the DSB test was used in this study as well according to the ISO/TS 17892-102 standard (ISO, S.T.E., 2019).

The test procedure and setup followed the method described by Head and Epps (1980) and Horváth et al. (2022). The test consisted of two phases: consolidation and shearing. In the consolidation phase, vertical (normal) pre-loads of 50, 100, and 150 kPa were applied to the soil samples. Vertical displacement was recorded over time until stabilization was observed, indicated by no further measurable movement. Once stabilized, the soil samples were sheared horizontally to a displacement of 6.5 mm. During this phase, the applied horizontal force was recorded to calculate the shear stress.

2.3. Cone penetration tests

Cone penetration tests were conducted as an analogue to earthworm burrowing, with a particular focus on how geometric features (e.g., cone half-angle, mouth opening corresponding to the center hole diameter) and lubrication affect penetration resistance in silt loam soil. By simulating different burrowing strategies (i.e., ingestion or cavity expansion) through custom-designed cones and controlled lubrication conditions, this study aims to quantify the energy efficiency of earthworm-like soil ingestion and penetration modes.

2.3.1. Cone design

To investigate the effects of mouth opening and tip angle on penetration resistance, six custom-designed steel cones were used. The cones included holes to represent the soil-ingestion burrowing mode observed in earthworms. The parameters of the cones are illustrated in Fig. 1. Two design parameters were varied: cone half-angle α (15° and 30°) and center hole diameter d (0, 2, and 5 mm). The cone outer diameter was kept constant as $D = 10$ mm. The cones are later referenced by cone half-angle and hole diameter. For example, cone (15°, 2 mm) refers to a cone with half-angle 15° and hole diameter 2 mm.

2.3.2. Earthworm mucus analogue

To examine the effect of lubrication (analogous to earthworm mucus) on penetration resistance, cones were coated with a 0.4% agar solution. Actual earthworm mucus was not collected. Instead, the agar solution was used as a proxy. Based on an assumed earthworm penetration speed of 10 mm/min (Ruiz et al., 2016) and mucus layer thickness of 0.1 mm (Zhang et al., 2016), the resulting shear rate was approximately $1.67\,s^{-1}$. Using power-law models and the Arrhenius equation, the apparent viscosity of the 0.4% agar solution is estimated to be 1.64–1.90 Pa · s at 22 °C temperature (Yu et al., 2020; Abchiche et al., 2020), which is comparable to the apparent viscosity of earthworm mucus under these conditions, which is in the range $0.37 - 1.90$ Pa · s (Zhang et al., 2016). Concentrations above 0.5% would form a gel already at 25°C (Asyakina and Dyshlyuk, 2016), making 0.4% a practical choice that mimics the viscosity of mucus while remaining fluid.

To prepare the lubricant, agar-agar powder (food-grade; C.L.T. Intertrade Co., Ltd.) was dissolved in boiling water and stirred until fully dissolved. The solution was applied in two ways: the cone tip was dipped entirely into the agar solution, and additional agar was injected through the hole to ensure internal lubrication. After dipping, the cones were held vertically and agar was also applied externally using a syringe to ensure uniform coverage. Finally, the cones were mounted onto the penetrometer using a custom adaptor for testing (see Fig. 2a).

2.3.3. Measurement procedure

For the CPT, each cone was tested in both silt loam soils under lubricated and dry conditions. Each cone configuration was tested three times in the low organic matter content soil and two times in the high organic matter content soil. To replicate earthworm burrowing behavior, the penetration speed was set to 10 mm/min (Ruiz et al., 2017). The maximum penetration depth for each cone was 35 mm, which was sufficient, as the penetration resistance stabilized after the first 15 mm in the low organic content silt loam soil. During penetration, resistance force and time were recorded and stored. As the cone was gradually withdrawn, it left a burrow in the soil sample. Once the cone was fully removed, a top-view image of the burrow was captured. For cones with holes, the tip conditions were documented after each test, and the soil collected inside the cone was dried in an oven at 105 °C for 24 hours and then weighed. The soil collected by the cones is later referred to as "ingested soil" as it is analogous to soil ingested by an earthworm.

To visualize burrow wall compaction, the burrows were dyed using a food grade dye. Based on Kasteel et al. (2005), brilliant blue FCF E133 was used, but with a modified concentration of 10 g/L (Eurodust Azure Food Coloring) for faster infiltration and reduced moisture loss. The dye solution was injected into the burrow using a rubber bulb syringe until the liquid level reached the soil surface. Infiltration was allowed to proceed for 1 h at room temperature (22 °C). If the dye level dropped, additional dye was added until the surface level was restored. After infiltration, excess dye was removed using a syringe, and the sample was inverted to drain remaining droplets. The metal rings were then left at room temperature for 1 h before photographing the top view of the dyed burrows.

Finally, to examine the dyed cross-sections, the soil sample was vertically cut along the burrow centerline using a stainless steel curved spatula, avoiding horizontal movement to prevent smearing. To facilitate removal from the metal ring, the soil samples were dried at 105 °C for 1 hour to dry the contact surfaces. Once removed, cross-sectional views were photographed for analysis of burrow wall dye infiltration and compaction.

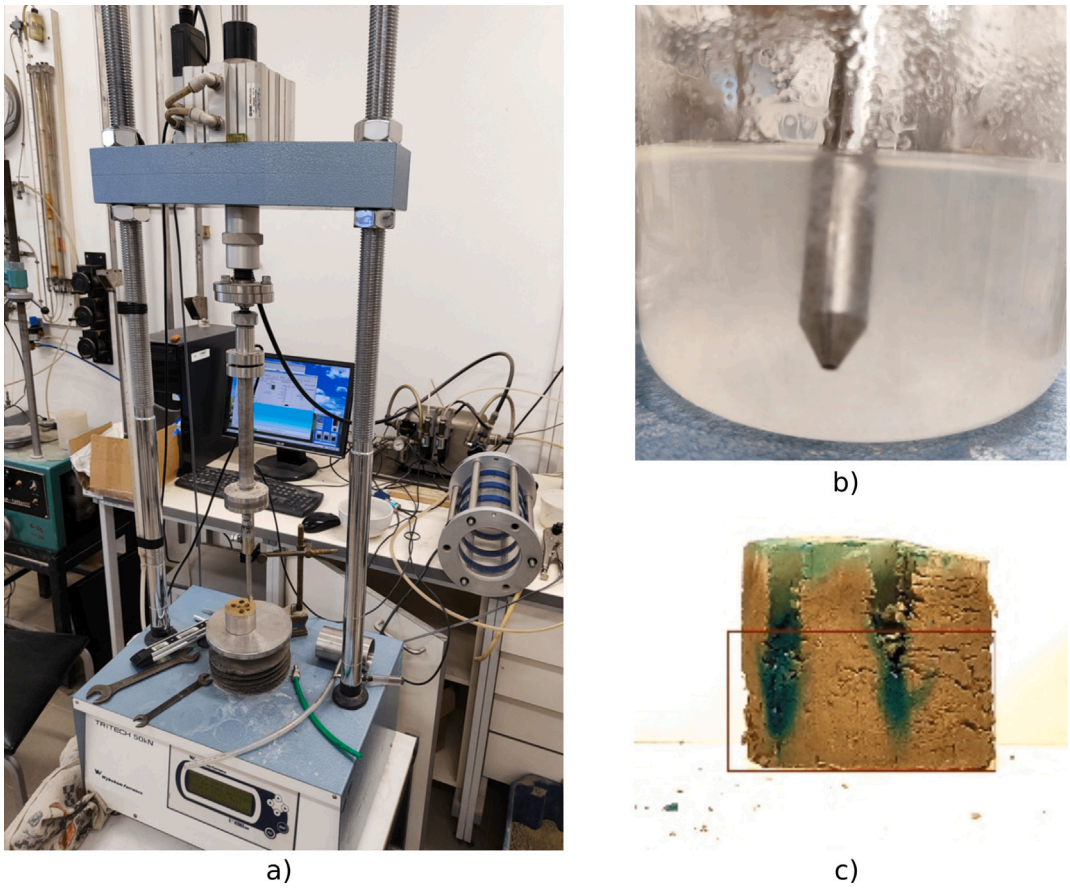

Fig. 2. (a) The penetrometer used for the CPT (Wykeham Farrance, Tritech 50 kN, Serial Number 09008294); (b) Lubrication of the steel cone with agar solution; (c) Cross-sectional view of the cone in ImageJ (version 1.54 g). The picture was edited for its white balance to get a clear dye infiltration pattern, and the red square represents the reference height of 25 mm.

2.3.4. Calculation of the energy balance

The energy balance of the cone penetration consists of two components: output and input. The output represents the energy consumed during cone penetration and corresponds to the minimum work required by an earthworm to penetrate the soil and create a burrow. The output energy (i.e., the energy required for burrowing) was found by integrating the penetration resistance over the penetration depth as

$$W = \int_0^{z_{\max}} F(z)\mathrm{d}z, \tag{1}$$

where $z_{\max} = 30\,\mathrm{mm}$ is the end of integration. The input, representing the energy available for the earthworm, was estimated based on the mass and organic carbon content of the soil ingested by the cone. From the point of view of an earthworm, the material flowing through the hole corresponds to the soil ingested by the earthworm. The organic matter in the ingested soil is converted into energy by the earthworm. The amount of energy obtained can be estimated from the organic matter density and the ingestion ability of the earthworm. The total energy intake of an earthworm is derived from the ingestion of soil containing organic matter, specifically organic carbon. This energy can be expressed as

$$E_{\mathrm{in,t}} = m \cdot c_{\mathrm{om}} \cdot f_{\mathrm{oc}} \cdot e_{\mathrm{oc}}, \tag{2}$$

where m is the mass of ingested soil, c_{om} is the mass fraction of total organic matter in the soil, $f_{\mathrm{oc}} = 0.58$ is the fraction of organic carbon within the organic matter (Pribyl, 2010), and $e_{\mathrm{oc}} = 35\,\mathrm{kJ/g}$ is the energy density of organic carbon. It was assumed that the organic matter is homogeneously distributed throughout the soil. The value of c_{om} depends on the soil type, as given previously in Table 1.

To estimate the biologically useful portion of this energy, the assimilation efficiency must be taken into account. This efficiency reflects the fraction of ingested organic carbon that is metabolically assimilated and available for biological functions, such as movement and burrowing. The assimilated energy, that is available for burrowing is therefore given by

$$E_{\mathrm{in,u}} = \eta \cdot E_{\mathrm{in,t}}, \tag{3}$$

where η is the assimilation efficiency (Martin et al., 1992). The assimilation efficiency of $\eta = 0.062$ was assumed based on soil organic carbon contents in bulk soil and casts of Arrázola-Vásquez et al. (2022).

2.4. DEM simulations

GPU-based DEM simulations were employed, utilizing parallelized computations for acceleration. We used the GPU-based DEM solver introduced by Nagy et al. (2024), which parallelizes the DEM computations by assigning each particle to a separate GPU thread, enabling the simultaneous calculations of forces, interactions, and displacements for thousands of particles. GPU-wide thread synchronization was applied to ensure computational accuracy. In this work, we extend the model of Nagy et al. (2024) by introducing a simplified treatment of adhesion and liquid bridge forces.

Particle–particle interactions were modeled using the Hertz–Mindlin contact theory, extended to account for sliding friction, rolling friction, liquid bridge forces, and adhesion. Although spherical particles were used, these parameters enable the model to capture the effects of particle angularity by representing interlocking and resistance to relative motion between particles. The contact between two particles

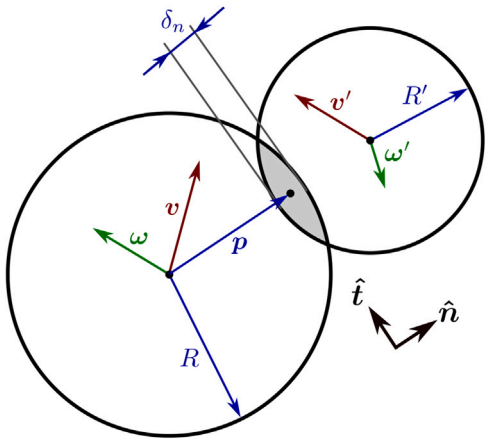

Fig. 3. Contact between two particles, where $\boldsymbol{v}$ is the velocity, $\boldsymbol{\omega}$ is the angular velocity, R is the radius of the particle, $\boldsymbol{p}$ is a vector that points into the point of contact and δ_n is the normal overlap. The prime notation ($\square'$) denotes the neighboring particle. The unit normal and tangential vector are given by $\hat{\boldsymbol{n}}$ and $\hat{\boldsymbol{\imath}}$, respectively.

is illustrated in Fig. 3, where $\boldsymbol{p}$ is the vector pointing from the center of the particle to the contact point, $\boldsymbol{v}$ is the particle velocity, and R is the particle radius. The normal overlap δ_n and the tangential overlap $\boldsymbol{\delta}_t$ are defined following Golshan et al. (2023) as:

$$\delta_n = (R + R') - d, \tag{4}$$

$$\boldsymbol{\delta}_t^{\{k+1\}} = \boldsymbol{\delta}_t^{\{k\}} + \Delta t \cdot \tilde{\boldsymbol{v}}_t, \quad \boldsymbol{\delta}_t^{\{0\}} = \boldsymbol{0}, \tag{5}$$

where R and R' are the radii of the two interacting particles, d is the center-to-center distance, Δt is the time step, and $\tilde{\boldsymbol{v}}_t$ is the tangential component of the relative velocity. The tangential overlap $\boldsymbol{\delta}_t$ is updated incrementally in time according to Eq. (5), where k denotes the time step index.

The total normal force between two particles is computed as the sum of elastic ($\boldsymbol{F}_{n,e}$), damping ($\boldsymbol{F}_{n,d}$), adhesion ($\boldsymbol{F}_{n,a}$), and liquid bridge ($\boldsymbol{F}_{n,lb}$) forces:

$$\boldsymbol{F}_n = \boldsymbol{F}_{n,e} + \boldsymbol{F}_{n,d} + \boldsymbol{F}_{n,a} + \boldsymbol{F}_{n,lb}. \tag{6}$$

The total tangential force is the sum of the elastic ($\boldsymbol{F}_{t,e}$) and damping ($\boldsymbol{F}_{t,d}$) components:

$$\boldsymbol{F}_t = \boldsymbol{F}_{t,e} + \boldsymbol{F}_{t,d}. \tag{7}$$

As the above force act at the contact point, the tangential force results in a torque as

$$\boldsymbol{M} = \boldsymbol{p} \times \boldsymbol{F}_t, \tag{8}$$

where $\boldsymbol{p}$ points to the contact point as depicted in Fig. 3. The remainder of this section details the formulations of each force component in Eqs. (6) and (7), as well as the implementation of frictional interactions.

2.4.1. Elastic and damping forces

The elastic and damping interactions between particles are computed using the Hertz–Mindlin contact model, which accounts for nonlinear elastic deformation and velocity-dependent energy dissipation. The normal and tangential components of the elastic and damping forces based on Cundall (1979) are given as:

$$\boldsymbol{F}_{n,e} = -\frac{4}{3} E^* \sqrt{R^*} \cdot \delta_n^{3/2} \cdot \hat{\boldsymbol{n}}, \tag{9}$$

$$\boldsymbol{F}_{t,e} = -S_t \cdot \boldsymbol{\delta}_t, \tag{10}$$

$$\boldsymbol{F}_{n,d} = -2\sqrt{\frac{5}{6}} \cdot \beta \cdot \sqrt{S_n \cdot m^*} \cdot \tilde{\boldsymbol{v}}_n, \tag{11}$$

$$\boldsymbol{F}_{t,d} = -2\sqrt{\frac{5}{6}} \cdot \beta \cdot \sqrt{S_t \cdot m^*} \cdot \tilde{\boldsymbol{v}}_t, \tag{12}$$

where δ_n is the normal overlap, $\boldsymbol{\delta}_t$ is the tangential displacement vector, $\tilde{\boldsymbol{v}}_n$ and $\tilde{\boldsymbol{v}}_t$ are the normal and tangential components of the relative velocity, and $\hat{\boldsymbol{n}}$ is the unit vector along the line connecting the particle centers. The stiffness terms are defined as

$$S_n = 2E^* \sqrt{R^* \delta_n}, \tag{13}$$

$$S_t = 2G^* \sqrt{R^* \delta_n}, \tag{14}$$

where E^* and G^* are the equivalent Young's and shear moduli, respectively, R^* is the equivalent radius, and m^* is the equivalent mass. All equivalent properties (E^*, G^*, R^*, and m^*) are calculated following the approach of Pásthy et al. (2022). The damping factor β, which determines the magnitude of the velocity dependent damping forces in the particle contacts, is derived from the coefficient of restitution e according to Tsuji et al. (1992) and Dhaouadi et al. (2022):

$$\beta = -\frac{\ln(e)}{\sqrt{\ln(e)^2 + \pi^2}}. \tag{15}$$

2.4.2. Adhesion force

Adhesion forces play a significant role in particle interactions, especially in fine or cohesive soils where surface forces cannot be neglected. In our simulations, adhesion is modeled using the Johnson–Kendall–Roberts (JKR) theory (Johnson et al., 1971), which accounts for elastic deformation and surface energy contributions during contact. The normal adhesion force is calculated as (Marshall, 2009; Kosaku et al., 2023):

$$\boldsymbol{F}_{n,a} = -\sqrt{16\pi \cdot \sigma \cdot E^* \cdot a^3} \cdot \hat{\boldsymbol{n}}, \tag{16}$$

where σ is the surface tension coefficient, E^* is the equivalent Young's modulus, and a is the contact radius. For computational efficiency, the contact radius is approximated as $a \approx \sqrt{R^* \delta_n}$, where R^* is the equivalent radius and δ_n is the normal overlap between the particles. This simplified form captures the essential behavior of cohesive interactions without requiring the solution of nonlinear equations via iteration.

2.4.3. Liquid bridge force

The liquid bridges counteract tensile forces and can also withstand torques; considering them is essential for accurately modeling wetted, cohesive soils (Tamás, 2018). The liquid bridge forces are also in effect when the particles are not in contact, that is, for $\delta_n < 0$ according to Eq. (4). The liquid bridge force acting in the normal direction between particles is (Kosaku et al., 2023):

$$\boldsymbol{F}_{n,lb} = -\frac{4\pi R^* \sigma \cos(\theta)}{1 + 1/\zeta} \cdot \hat{\boldsymbol{n}}, \tag{17}$$

where σ is the surface tension coefficient and θ is the contact angle. The coefficient ζ is calculated as (Israelachvili, 2011):

$$\zeta = \sqrt{1 + \frac{2V_L}{\pi R \delta_n^2}} - 1, \tag{18}$$

where V_L is the volume of the liquid bridge between particles. We define a new parameter Ψ, which gives the average liquid film thickness around the particles:

$$\Psi = \frac{V_{L,\mathrm{t}}}{S_{\mathrm{t}}}, \tag{19}$$

where $V_{L,\mathrm{t}}$ is the total liquid content of the system and S_{t} is the total surface area of all particles. The volume of a liquid bridge is approximated from the average film thickness Ψ as

$$V_L \approx \frac{4\pi\Psi(R^2 + R'^2)}{\overline{N}_c}, \tag{20}$$

where $\overline{N}_c$ is the average coordination number. This approximation holds for nearly equally sized particles. A liquid bridge is considered to form between particles if $\delta_n > -\Psi$, that is,

$$d < R + R' + \Psi, \tag{21}$$

where R and R' are the neighboring particle radii, and d is the distance between particle centers.

2.4.4. Friction forces

The static friction and the sliding friction are implemented based on Pásthy et al. (2022), Nagy et al. (2024). Particles slip on each other if the tangential force is too large

$$|\boldsymbol{F}_t| > \mu_0^* \cdot |\boldsymbol{F}_n|. \tag{22}$$

In this case, the magnitude of the tangential force is limited to $|\boldsymbol{F}_t| = \mu^* |\boldsymbol{F}_n|$, where μ^* is the equivalent sliding friction coefficient and μ_0^* is the equivalent static friction coefficient. The rolling friction results in a torque in the direction against the angular velocity vector (Solutions, 2014),

$$\boldsymbol{M}_\mu = -\mu_r^* \cdot |\boldsymbol{F}_n| \cdot |\boldsymbol{p}_{1,2}| \cdot \frac{\boldsymbol{\omega}}{|\boldsymbol{\omega}|}, \tag{23}$$

where μ_r^* is the equivalent rolling friction coefficient. To account for the rolling friction during the simulations, the torque acting on the particle in Eq. (8) is incremented with $\boldsymbol{M}_\mu$.

2.5. Setup and evaluation of DEM simulations

GPU-accelerated DEM simulations were conducted to calibrate micromechanical parameters and reproduce cone penetration tests. The setup and evaluation steps of the DEM simulations are discussed below.

2.5.1. Direct shear box tests

To accelerate the calibration process, the width of the simulated shear box was reduced from 60 mm to 6 mm. A total of 26 240 particles were simulated, with particle sizes uniformly distributed in the range $R = 0.3 \ldots 0.5$ mm. First, a partially deposited particle assembly was created. This assembly was then compressed by a plate pushed downward with a force corresponding to the desired normal load (50, 100, or 150 kPa), defined as:

$$F_n = \sigma_n \cdot A_{\text{red}}, \tag{24}$$

where σ_n is the normal load and $A_{\text{red}} = 6 \times 60\,\text{mm}^2$ is the reduced contact area. The DEM simulations then continued until the plate reached equilibrium. Once equilibrium was achieved, shearing began at a constant shear velocity (v_s), and the corresponding shear force (F_s) was recorded. Then, from the shear force the shear stress could be found for the full shear box as

$$\tau_{\text{DSB}} = \frac{10 F_s}{A}, \tag{25}$$

where $A = 60 \times 60\,\text{mm}^2$. The results of these shear box simulations serve as the basis for parameter calibration and are discussed in Section 3.

2.5.2. Cone penetration tests

Throughout the cone penetration simulations, the same particle size and size distribution were used as in the DSB validation phase (that is $R = 0.3 \ldots 0.5$ mm with a uniform distribution). Each simulation initially contained 51 200 particles. The time step size was set to 2 µs and the simulation length was 2 s. In the first half of the simulation the cone was inserted with 30 mm/s, while in the second half it was withdrawn with 40 mm/s. Altogether, 1 million time steps were taken, which took approximately one hour on an NVIDIA RTX 3060 Ti graphics card. Decreasing the penetration velocity did not show any meaningful difference; thus, using a penetration velocity higher than in experiments was justified. The effect of penetration velocity is investigated in detail in Appendix B.

Calculation of the porosity

The simulation domain had a cross-sectional area of $26 \times 26\,\text{mm}^2$, while the particle bed depth (depending on porosity) ranged from 30 … 40 mm, comparable to the experimental setup. To achieve different soil porosities, the soil was compacted from above at a constant velocity until the desired density was reached. We define the porosity as

$$\phi = \frac{V_{\text{void}}}{V_{\text{total}}}, \tag{26}$$

where V_{void} is the void volume and V_{total} is the total volume. Four different particle assemblies were prepared for the low organic matter content silt loam soil, with porosities of $\phi = 20\%$, 25%, 30%, and 36%.

Evaluation of the soil density

In the simulations, we approximated the local soil density using the relative particle density. The relative particle density as a function of distance from the centerline of the cone was defined as follows:

$$\hat{\rho}(r) = \frac{N_r / V_r}{\rho_{\text{ref}}} \tag{27}$$

where r is the distance from the centerline of the cone, V_r is the volume between two concentric cones with radii $r \pm \Delta r/2$, given by

$$V_r = \pi \left[\left(r + \frac{\Delta r}{2} \right)^2 - \left(r - \frac{\Delta r}{2} \right)^2 \right] \cdot (z_{\max} - z_{\min}). \tag{28}$$

The number of particles located within this volume is denoted by N_r. The reference density is defined as the ratio of the total number of particles (N_{total}) to the initial volume of the soil sample (V_{total}), that is, $\rho_{\text{ref}} = N_{\text{total}}/V_{\text{total}}$. The soil density was calculated within a slice defined by $z_{\min} = 15$ mm and $z_{\max} = 25$ mm to avoid boundary effects from the top and bottom of the domain.

Soil collected by the cones

The DEM simulations allowed the quantification of ingested soil mass in two distinct states: (i) at maximum penetration ($m_{\max}^{\text{sim}}$), representing the mass of soil confined inside the cone cavity, and (ii) after the cone was slowly withdrawn, representing the residual mass retained in the cone ($m_{\text{end}}^{\text{sim}}$). The ingested soil for the two cases was calculated by summing the mass of each particle in the cone hole. It should be noted that the soil ingestion in CPT represents a mechanical analogue and does not capture the active, peristaltic suction or periodic feeding motions of real earthworms. To facilitate comparison with the measurements, the dry soil mass was calculated by reducing the total mass by 25%, accounting for water loss during drying. This correction was reasonable, as the DEM model does not inherently include moisture; instead, moisture effects were indirectly captured through the micromechanical parameters determined during the validation process. The validation was done with the same soil with 25% water content. From the dry soil mass, the energy available for the earthworm was calculated in the same way as in the measurements, following Section 2.3.4.

3. Calibration of DEM simulations via direct shear box tests

The direct shear box (DSB) test was used to calibrate micromechanical soil parameters for the CPT DEM simulations. Since the simulated soil particles are necessarily much larger than real grains, the goal of the calibration is to reproduce the correct macro-scale behavior of the soil, even though this may result in micromechanical parameters that do not directly correspond to those of the actual soil particles. A straightforward calibration method was applied: a list is defined for each micromechanical parameter, and all parameter combinations were tested. Due to the efficient GPU implementation, hundreds of parameter combinations could be tested within a day on a single GPU device. The resulting database was then used to identify the best-fitting parameters for the soils.

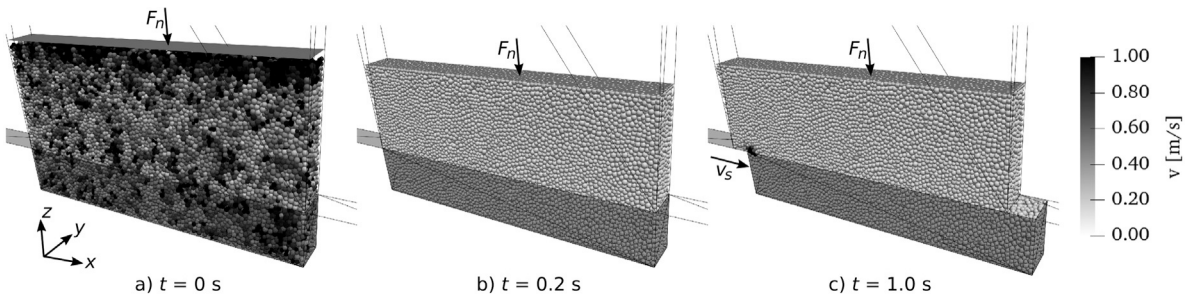

Fig. 4. DSB test using DEM. (a) Initial particle assembly in the shear box. (b) Settled particle assembly before the start of shearing. (c) Shearing phase with shear velocity $v_s = 5\,\text{mm/s}$. Particles are colored based on velocity magnitude, as indicated by the color scale on the right.

Table 2
Micromechanical DEM parameter combinations for the calibration simulations.

Parameter	Notation	Values	Unit
Particle density	ρ	2200	kg/m^3
Young's modulus	E	40, 80, 120, 160	MPa
Poisson's ratio	ν	0.25	1
Sliding friction coeff.	μ	0.05, 0.1, 0.2, 0.4	1
Rolling friction coeff.	μ_r	0.05	1
Coeff. of restitution	e	0.4, 0.6, 0.8	1
Surface tension coeff.	σ	15, 20, 25, 30, 35, 40	N/m
Avg. liquid film thickness	Ψ	0.006	mm
Contact angle	θ	0.1	rad

Table 3
Best fitting micromechanical DEM parameters for silt loam soil with various organic matter content.

Parameter	Notation	Unit	Organic matter content	
			Low	High
Young's modulus	E	MPa	80	80
Sliding friction coeff.	μ	1	0.1	0.4
Coeff. of restitution	e	1	0.6	0.4
Surface tension coeff.	σ	N/m	40	40
Fit quality	Q		88.2%	86.2%

A representative simulation of the DSB test is given in Fig. 4. The simulations began from a partially deposited assembly as depicted in Fig. 4a. Then, simulations continued until the plate reached equilibrium, as depicted in Fig. 4b. Once equilibrium was achieved, shearing began at a constant shear velocity, as illustrated in Fig. 4c.

Initial parameter studies were conducted to identify realistic and numerically stable ranges for the DEM parameters. We found that high Young's modulus values ($E \geq 200\,\text{MPa}$) often led to numerical instabilities, and therefore the upper limit was restricted accordingly. For the surface tension parameter, large values caused particle clusters; thus, we limited the range to $\sigma \leq 40\,\text{N/m}$. At the same time, relatively high surface tension values were still required to reflect the substantial soil cohesion influencing the measured shear forces. The rolling resistance coefficient and contact angle were found to have only a weak influence on the shear response in preliminary tests, and these parameters were therefore kept constant during calibration. Finally, reasonable and physically meaningful ranges were selected for the sliding friction coefficient and the coefficient of restitution, as initial tests suggested higher sensitivity to these parameters. Based on these initial tests, the parameter ranges were identified, in which good agreement with experimental measurements was achievable. The fixed parameters and parameter ranges are listed in Table 2, altogether 288 parameter combinations are possible based on the data in the table. For each possible combination of parameters, a DEM simulation was performed for all three normal loads (50, 100, and 150 kPa). The three load cases for a single parameter combination required approximately 10 min of computation time on a commercial NVIDIA RTX 3060 Ti graphics card. The shear velocity was set to $v_s = 20\,\text{mm/s}$, and the time step size to $\Delta t = 2\,\mu\text{s}$. As shown in Appendix A, further decreasing the time step size or the shear velocity does not significantly affect the results; thus, using a shear velocity larger than in the measurements can be justified.

The quality of the fit between simulation and experiment was evaluated using the L_2 norm of the relative error:

$$L_2\left\{F_{s,\sigma_n}(x)\right\} = \sqrt{\frac{1}{x_{\max}}\int_0^{x_{\max}}\left(\frac{\tilde{F}_{s,\sigma_n}(x) - F_{s,\sigma_n}(x)}{\tilde{F}_{s,\sigma_n}(x)}\right)^2 \mathrm{d}x}, \tag{29}$$

where $x_{\max}$ is the maximum shear displacement, $F_{s,\sigma_n}(x)$ is the simulated shear force for normal stress σ_n, and $\tilde{F}_{s,\sigma_n}(x)$ is the corresponding experimental curve. The overall fit quality for each parameter combination was quantified by the mean L_2 error across the three load cases:

$$Q = 1 - \frac{L_2\left\{F_{s,50\,\text{kPa}}(x)\right\} + L_2\left\{F_{s,100\,\text{kPa}}(x)\right\} + L_2\left\{F_{s,150\,\text{kPa}}(x)\right\}}{3}, \tag{30}$$

where Q denotes the fit quality. A Q closer to 1 indicates a better match with experimental results. The best-fit parameters for the two different silt loam soils are listed in Table 3. The best-fitting simulation results are compared to the experimental displacement–shear force curve in Fig. 5.

Although the fit qualities are relatively high based on the definition in Eq. (30), above 85% in both cases as given in Table 2, there are a few qualitative differences, as depicted in Fig. 5. For low organic matter content silt loam soil (Fig. 5a), the initial steepness of the curve is underpredicted under higher normal loads (see the blue and green curves). For the high organic matter content silt loam soil, the maximum shear force at the highest load (150 kPa) is significantly underpredicted, as depicted by the green curve in Fig. 5b.

In general, the required shear force (and shear stress) increases linearly with the normal load in the DEM simulations (Zeraati-Shamsabadi and Sadrekarimi, 2025). However, this is not true for all soil types; therefore, such behavior cannot be reproduced by the DEM simulations, at least not with the type of modeling described in Section 2.4. Despite these qualitative differences, the fit quality based on Eq. (30) remains high, because two of the curves consistently fit well to the experimental data, and the fit quality Q is based on the average of the errors.

Compared to similar studies, the fit presented above can be regarded as excellent. Bernhardt et al. (2016) compared DEM simulations with DSB measurements using spherical ball bearings and achieved similar fit quality. Nitka and Grabowski (2021) compared simulations to DSB measurements for a cohesionless soil and reported a 2.5% error at the stress peak and a 10% error in the residual stress ratio. Nonetheless, the results presented in this study still suffer from some known limitations. Horváth et al. (2022) were also unable to calibrate micromechanical DEM parameters to describe the nonlinear dependence of normal load and maximum shear stress for hulled millet.

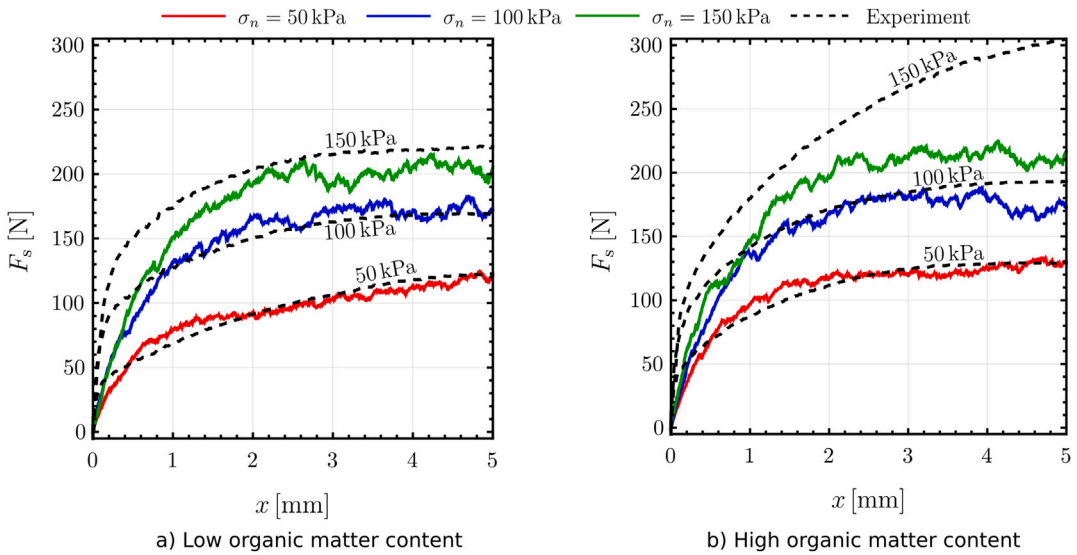

Fig. 5. Comparison of DEM simulation results with experimental data of the displacement–shear force curve. The parameters are given in Table 3.

4. Cone penetration test measurements and simulations

Cone Penetration Tests (CPT) were performed to model earthworm burrowing. First, the simulation settings are described, followed by the presentation and joint discussion of simulation and experimental results. The analysis focuses on the resistance force, the soil flowing into the cone holes mimicking earthworm ingestion, the soil density after cone penetration and the input and output energy. The input energy represents assimilated energy from soil ingestion, while the output energy corresponds to the energy expended during burrowing. Since the best agreement was found for low organic content silt loam soil in the direct shear box measurement and simulation, this is selected for the detailed presentation of the results. Results for high organic content silt loam soil are discussed in Appendix C. The results of the DEM simulations are presented in Fig. 6 and compared to the burrow profile following the experiments. The differences in the flow of soil into the cone center hole are visible. Particularly interesting is the difference between cone $(30°, 2\,\text{mm})$ and cone $(15°, 2\,\text{mm})$. In the case of cone $(30°, 2\,\text{mm})$ the flow of particles into the cone center hole is continuous, while for cone $(15°, 2\,\text{mm})$ it is not. For more pointy cones with cone half-angle 15°, the bottom of the burrow has a correspondingly smaller angle as expected.

4.1. Penetration resistance

First, the penetration resistance in the simulations and measurements is compared. Fig. 7 shows the required resistance force for cone $(30°, 0\,\text{mm})$ and cone $(30°, 2\,\text{mm})$ in silt loam soil with various porosities. The black line represents the average of the experimental measurements, while the gray shaded region indicates the standard deviation. The porosity of the silt loam soil in the experiment was estimated to be around 32% based on the particle density and bulk density. Among the simulated cases, the DEM results best match the experimental data when the porosity is 30%.

It can be observed that penetration into soil with lower porosity requires a higher force. This is because at lower porosity, the particles have less space to move and must compress each other, which demands more force. This effect is further analyzed in Fig. 8, which shows the required resistance force as a function of porosity for selected cones. In each case, a linear relationship is observed between porosity and the required pushing force, as indicated by the DEM simulations. Furthermore, the figure shows that for cones with larger holes, the required resistance force is lower.

4.2. Soil density around the burrow

Soil density can be easily measured locally in DEM simulations; however, it is much more difficult to assess in laboratory experiments. Instead of direct laboratory measurement, dye infiltration was used to gain a qualitative understanding. The extent and continuity of dye infiltration reflect differences in pore connectivity, which is influenced by local soil compaction. Regions where dye movement is restricted can be interpreted as denser zones, providing an indirect comparison to DEM. Fig. 9 shows the soil density during and after cone penetration in low organic content silt loam soil for cone $(30°, 0\,\text{mm})$ and cone $(30°, 2\,\text{mm})$.

Initially, the density is nearly homogeneous, as indicated by the red curve. Since cone $(30°, 0\,\text{mm})$ is solid and has no center hole, it completely displaces the particles within the reference zone at full penetration, as shown by the green curve. Fig. 9b presents the soil density around cone $(30°, 2\,\text{mm})$ in silt loam soil, which features a 2 mm center hole. As a result, the soil density remains higher near the center ($r \approx 0$) during penetration, and even following cone removal, as some particles fall back to the bottom of the hole. The brilliant blue FCF dye used in the experiments shows that the infiltration width is limited, and only the burrow wall is stained. This indicates that the surrounding soil remains compact after penetration, which is consistent with the results of the DEM simulations.

After cone withdrawal, the burrow slightly contracts while the surrounding soil expands, as shown by the orange curve in Fig. 9a-b. This indicates that the burrow wall relaxes and residual stresses remain minimal in the adjacent soil. Fig. 10 presents the stress vectors near the cone tip during penetration and after withdrawal for cones $(30°, 0\,\text{mm})$ and $(30°, 2\,\text{mm})$. The largest stresses occur directly below the cone during penetration (even up to 50 kPa as depicted in Fig. 10), while localized high stresses also appear along the burrow wall where shear takes place. After withdrawal, stresses near the wall are substantially reduced, as expected. However, at the bottom of the domain, the soil cannot expand freely, so residual stresses remain higher in this region.

4.3. Soil collected by the cones

Table 4 summarizes the mass of soil collected by the cones. For cones with a 2 mm hole, multiple cone half-angles were tested. In general, a good qualitative agreement is observed between the simulations and experiments for cones with small holes: minimal soil remains in the cone after it is withdrawn, and the retained mass increases with

Table 4
Soil "ingested" by the cones in the cone penetration test in low organic matter content silt loam soil and the energy requirement. The first two columns provide details of each cone: the hole diameter d, and cone half-angle α. The next two columns report the mass of soil collected during experiments for both dry ($m^{\mathrm{exp}}_{\mathrm{dry}}$) and lubricated ($m^{\mathrm{exp}}_{\mathrm{lub}}$) cases. Then, the next two columns show the mass inside the cone as determined from the DEM simulations: at maximum penetration ($m^{\mathrm{sim}}_{\mathrm{max}}$) and after cone removal ($m^{\mathrm{sim}}_{\mathrm{end}}$). The last three columns show the output work in the experiment (W^{exp}), simulation (W^{sim}) and the assimilated energy (useful input energy) in the simulation ($E^{\mathrm{sim}}_{\mathrm{in,u}}$).

d [mm]	α [deg]	$m^{\mathrm{exp}}_{\mathrm{dry}}$ [g]	$m^{\mathrm{exp}}_{\mathrm{lub}}$ [g]	$m^{\mathrm{sim}}_{\mathrm{end}}$ [g]	$m^{\mathrm{sim}}_{\mathrm{max}}$ [g]	W^{exp} [J]	W^{sim} [J]	$E^{\mathrm{sim}}_{\mathrm{in,u}}$ [J]
0	15°	–	–	–	–	0.291 ± 0.037	0.154	0.000
0	30°	–	–	–	–	0.271 ± 0.021	0.271	0.000
2	10°	–	–	0.008	0.028	–	0.120	0.555
2	15°	0.00	0.00	0.013	0.038	0.253 ± 0.048	0.168	0.750
2	20°	–	–	0.025	0.047	–	0.232	0.945
2	25°	–	–	0.056	0.070	–	0.278	1.396
2	30°	0.03	0.00	0.041	0.080	0.308 ± 0.035	0.316	1.591
2	45°	–	–	0.062	0.081	–	0.411	1.621
5	15°	0.21	0.47	0.000	0.633	0.323 ± 0.078	0.148	12.682
5	30°	0.65	0.78	0.000	0.628	0.394 ± 0.071	0.255	12.562

the cone half-angle. This trend can be explained by analyzing the particle flow during penetration, as shown in Fig. 6. In the case of cone (30°, 2 mm), there is an almost continuous inflow of particles into the hole. In contrast, for cone (15°, 2 mm), which has a sharper ending, more particles are pushed aside, resulting in a less continuous inflow and fewer particles reaching the region where the center hole widens (which is analogous to the gut of the earthworm). Therefore, during the burrowing of the earthworm, the earthworm is assumed to contract its circular muscle to form a sharp tip for the cavity expansion and to contract its longitudinal muscle to form a more blunt tip to squeeze soil and have a continuous flow into its mouth for the soil ingestion.

Most of the particles entering the narrow 2 mm section fall back into the soil sample, and only those that reach the gut tend to remain inside the cone. For cones (15°, 5 mm) and (30°, 5 mm), the soil did not remain inside the cone upon removal; instead, it fell back into the surrounding soil. This behavior was also observed in laboratory experiments, where no soil remained inside the cone after withdrawal (see, for example, Fig. 11e). This phenomenon is reminiscent of the *soil plug* effect known in pipeline installation, where part of the soil column is sheared away and falls out during extraction (Randolph et al., 1992). Understanding whether earthworms exploit such a passive "negative" ingestion mechanism, or whether they always rely on actively drawing soil in using their pharynx, requires further study. If the negative mechanism dominates, maximizing the mouth opening would be most effective, whereas for the active mechanism, the optimal hole size should ensure efficient suction while maintaining soil retention.

4.4. Energy balance

The last three columns of Table 4 present the experimentally measured penetration work, the simulated penetration work, and the assimilated energy (useful input energy) available to the earthworm. The assimilated energy (input) is calculated using Eqs. (2) and (3), based on the mass of soil flowing through the cone cavity ($m^{\mathrm{sim}}_{\mathrm{max}}$). The results indicate that, for each investigated cone design with $d > 0$ (with a hole), the earthworm would be able to penetrate the silt loam soil, as $E_{\mathrm{in,u}} > W$, assuming an assimilation efficiency of $\eta = 0.062$. The dependence of this result on design parameters is analyzed in detail in the following sections.

4.5. Effect of hole diameter

Measurements and DEM simulations were conducted using cones with hole diameters of 0, 2, and 5 mm. The results for silt loam soil with cone half-angles of 30° are summarized in Fig. 11, which presents the resistance force, the relative soil density after penetration, and top view images of the cone cavities following removal. Fig. 11a shows the measured and simulated penetration resistance force as a function of displacement. Two regions can be separated: a quasi-steady region, when the top of the cone is fully inside the soil characterized by a slowly increasing penetration force, and an initial transient phase as the cone penetrates the soil characterized by a monotonic increase in the penetration force with a larger gradient. As expected from the simulations, cones with larger holes experience reduced resistance forces in the steady region, since less material needs to be displaced. In the initial phase of penetration, cones with smaller hole diameters exhibit lower resistance forces because they are more pointed and have smaller contact areas in that phase. The simulation results match the experimental trends and magnitudes well in this early phase. However, in the quasi-steady region, the same trend is not consistently observed in the experiments. In the latter region, differences in the slope are likely caused by the cone–soil contact effects and soil inhomogeneity. Continuous cone contact causes the force to rise steadily, with slope variations arising from differences in effective friction, likely due to small water content differences during preparation and due to soil plug shear and plug–cone wall friction.

Fig. 11b presents the relative soil density after penetration as a function of the radial distance from the cone axis. For cone (30°, 0 mm), the soil is almost entirely displaced from the central region, resulting in a wide cavity with low density near the center ($r \approx 0$). For cone (30°, 2 mm), the central density is somewhat higher, indicating that some material remains or is less displaced. In the case of cone (30°, 5 mm), a significant amount of soil remains in the central region. Panels (c)–(e) of Fig. 11 show top view images of the soil after the cones were removed in the laboratory measurements and DEM simulations. For cone (30°, 0 mm) the burrow is clean, with most displaced soil remaining outside the burrow both in the experiments and simulations. A similar pattern is observed for cone (30°, 2 mm). In contrast, for cone (30°, 5 mm), the soil collected inside the cone during penetration remains in the burrow after removal, indicating that the friction between the cone wall and the particles is low enough for them to fall out as the cone is withdrawn. The cracks forming around the burrow are either radial or circumferential in the measurements. Their detailed characterization, as well as the investigation of the constructed soil's inter- and intra-aggregate pore network and its effect on mass transfer is possible (Barbosa and Gerke, 2023), however, beyond the scope of the current work. The simulations do not show crack formation, as these cracks are expected to be at least an order of magnitude smaller than the particle in the DEM simulations.

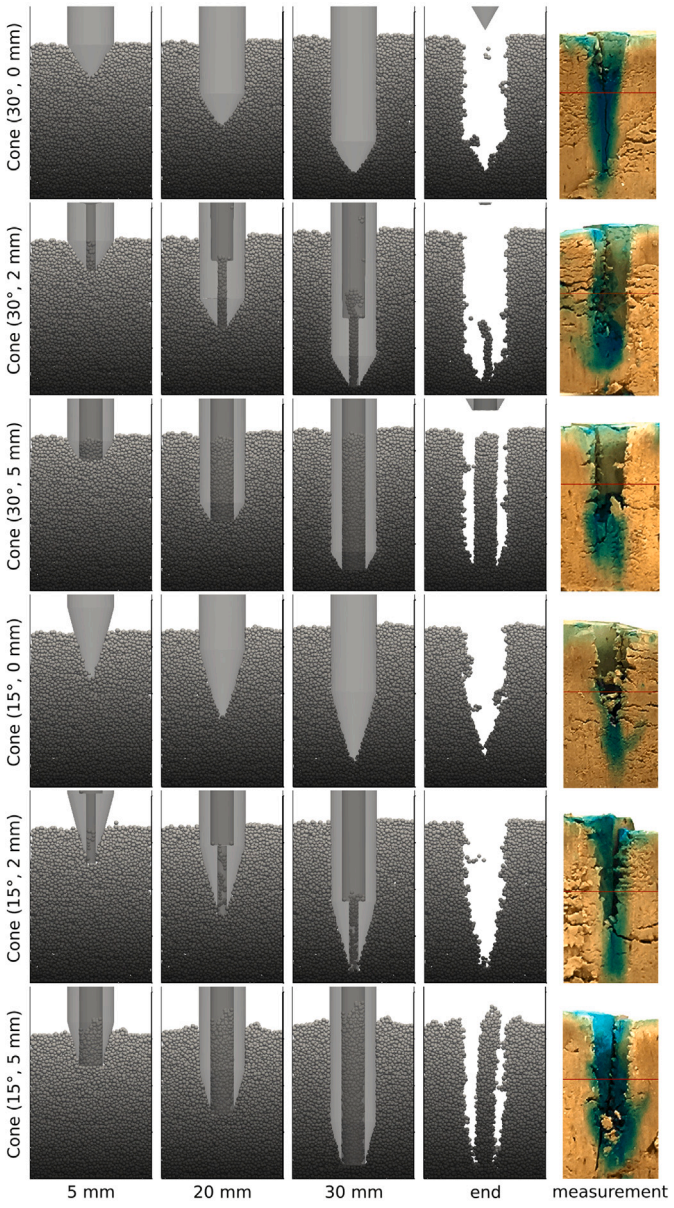

Fig. 6. DEM simulations in low organic matter content silt loam soil compared with experimental measurements. The first three columns correspond to 5 mm, 20 mm, and 30 mm penetration depths of the cone. The fourth column shows the final state after the cone has been slowly removed. The last column depicts the burrow from the experimental measurement following the dyeing of the burrow.

The data in Table 4 indicate that more soil is ingested by cones with larger holes, as expected intuitively. Consequently, the available energy derived from the organic matter in the ingested soil also increases with hole diameter. For a hole diameter of 5 mm, the available energy exceeds the required penetration work by two orders of magnitude. In summary, increasing the hole diameter reduces the required penetration force and alters the flow and redistribution of soil particles. The DEM simulations capture these trends effectively. Notably, the simulations reproduce the observation that for larger holes, particles tend to remain inside the burrow, as also demonstrated in Fig. 6 for cone (30°, 5 mm). While for small holes soil remains inside the cavity of the cone representing the gut of the earthworm, in both the experiments and simulations.

4.6. Effect of cone half-angle

The influence of the cone half-angle on soil penetration was investigated using DEM simulations for angles ranging from 10° to 45° with center hole diameter 2 mm mimicking the mouth of an earthworm. Experimental data is available for cone half-angles 15° and 30°. The results are presented in Fig. 12, showing the penetration resistance force and the relative soil density after cone removal.

Fig. 12a illustrates that cones with larger angles experience higher resistance forces, particularly in the steady penetration phase. Additionally, the initial slope of the force–displacement curve is steeper for larger angles, indicating the faster buildup of resistance during the early stage of penetration. This trend is consistent with physical intuition: wider cones displace more soil and thus require a larger force to advance. The experimental data for 15° and 30° follow a similar trend, although quantitative agreement is limited due to the variability and inhomogeneity of the soil samples. During the quasi-steady stage, the rate of resistance increase is mainly governed by the growth of the cone–soil contact area. In principle, if the friction coefficient and limiting surface pressure are constant the slope should be similar for different cone half-angles. However, the experimental data show a faster increase for the 15° cone, which may be explained by higher lateral compression and thus larger normal forces along its sides, leading to greater friction.

Fig. 12b shows the relative soil density as a function of radial distance from the cone axis. As the cone half-angle increases, a larger portion of the soil remains along the central axis rather than being displaced sideways. This results in more material being squeezed into the cone's cavity, as seen in the simulations, where the 30° cone exhibits a continuous inward soil flow, while the 15° cone does not, as demonstrated in Fig. 6. For the most pointed cone (10°), a significant amount of material remains near the axis at the bottom of the burrow, resulting in a narrower cavity and less displacement of soil. Pointed cones such as the 10° influence the local soil density less, since the total inserted volume in this case is also reduced. In summary, cones with larger angles displace more soil and require higher penetration forces. They also lead to greater soil compaction.

Correspondingly, the work required for penetration should increase with larger cone half-angles. This is verified in Table 4 for DEM simulation for all cones and also by measurement data for cone (30°, 2 mm) and (15°, 2 mm). Although the mechanical work increases in the simulations, the energy gained from ingesting the soil also increases with the cone half-angle. This trend is partially supported by the experimental measurements: for a 15° cone, very little soil remains inside the cone after penetration (measured as 0 g), whereas for the larger 30° cone, this increases to 0.03 g, which is comparable to the amount of soil that remains in the cone cavity after withdrawal (0.041 g). This indicates that evaluating only the penetration force is insufficient for identifying optimal burrowing strategies. The amount of ingested soil and thus the energy that can be metabolically recovered must also be taken into account. Based on the data in Table 4, we can identify the optimal burrowing strategy in silt loam soil assuming a 2 mm hole diameter: the ratio between the available energy for burrowing ($E_{\mathrm{in,u}}$) and the required work (W) reaches a maximum of 5 for cone half-angles in the range of 25°–30°. For other cone angles, this ratio remains below 4.6. This suggests that cone half-angles of 25°–30° are energetically optimal, meaning that in these cases, up to five times more energy is available for burrowing than is required to overcome the resistance.

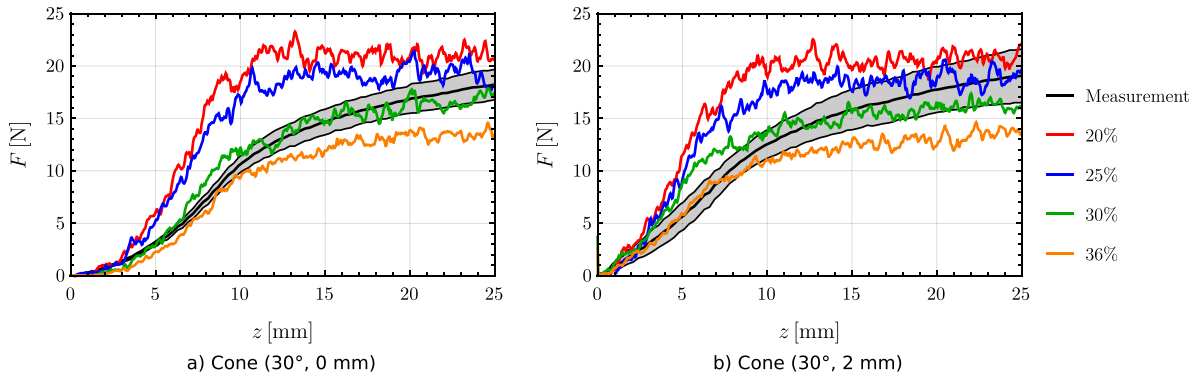

Fig. 7. Comparison of DEM simulation results with experimental displacement z – resistance force F curves in low organic content silt loam soil at various porosities, as indicated in the legend. The black line represents the average of the measurements, and the gray shaded area corresponds to the standard deviation.

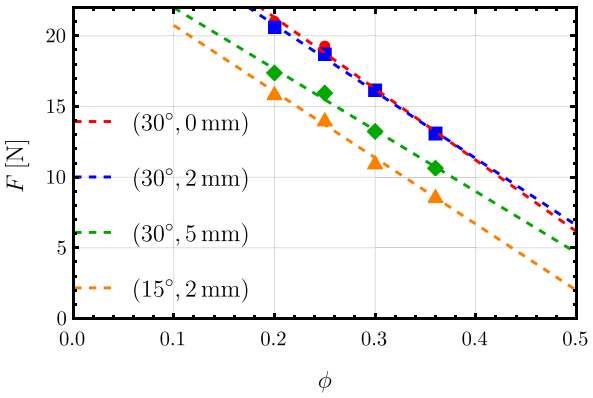

Fig. 8. Penetration resistance force F as a function of porosity ϕ with various cones in silt loam soil. The legend shows the center hole diameter and cone half-angle.

4.7. Effect of lubrication

In low organic content silt loam soil, lubrication had little impact on the measured resistance force, as depicted in Fig. 13a. In the DEM simulations, the sliding friction coefficient between the particles and the cone was varied; however, this hardly affected the penetration resistance. For this reason, only a single curve is shown for the DEM simulations. Overall, there is good qualitative agreement between the measurements and simulations regarding the effect of lubrication in low organic soil. Additionally, in the measurements, lubrication slightly influenced the amount of soil "ingested" by the cones in low organic content silt loam, as summarized in Table 4. In high organic content soil, experimental data suggest a slight decrease in penetration resistance (Fig. 13b). Across the six tested cone geometries, the work required for penetration decreased by approximately 11% due to lubrication, although this effect was not captured by the DEM simulations. Overall, these results indicate that earthworm mucus has a limited effect on penetration resistance and the overall energy balance.

5. Discussion

The simulations indicate a generally linear relationship between soil porosity and the resistance force during penetration, which appears largely independent of lubrication effects. This suggests that, at least in low organic content silt loam soils, the frictional interaction between the cone (or earthworm) and the soil is primarily governed by geometrical constraints and particle rearrangements, rather than by the presence of water or mucus. Such a finding implies that the energy cost of burrowing may be predictable based on the initial soil packing, independent of moisture effects under the tested conditions. These findings are in line with previous DEM-based CPT studies that also predict a linear relationship between porosity and penetration resistance (Ciantia et al., 2016). Experimental CPT measurements of some soils can show more complex behavior (Ghali et al., 2019), but capturing such non-linearity would require more sophisticated DEM modeling.

The local soil density around the penetrating cone was observed to increase by roughly 10% during the passage, reflecting compaction in the immediate surroundings. After the cone or earthworm leaves the domain, the density at the penetration site is reduced, indicating the relaxation of the disturbed soil. This phenomenon suggests that earthworm burrowing not only displaces soil but also temporarily modifies the local soil structure, which could influence subsequent burrowing passages or root and water transport.

The cone center hole diameter is a key factor in determining the amount of soil ingested. Larger openings allow more soil to be forced into the cone cavity, thereby increasing the energy available to the earthworm. However, excessively large mouth openings are constrained by the body size of earthworms. This trend was consistently observed in both simulations and experiments. For wider holes, soil tended to remain in the burrow rather than adhering to the cone upon withdrawal. This behavior resembles the well-known soil plug effect in pipeline installation, where part of the soil column remains inside the pipe. It should be noted that the CPT measurements and the DEM simulations represent this as a passive filling of the cone cavity and do not account for active pharyngeal suction or peristaltic feeding by the earthworm, which may alter soil intake dynamics. Whether earthworms take advantage of such a passive "negative" ingestion mechanism, or instead rely primarily on actively drawing soil in with their pharynx, remains an open question. If the passive mechanism plays a dominant role, a larger mouth opening would be more effective. In contrast, if active suction is critical, an optimal hole size must balance efficient ingestion with the ability to retain soil within the burrow. Future research could explore this hypothetical mechanism by which earthworms actively suck soil into their mouths, as opposed to relying solely on passive displacement, to better replicate natural feeding behavior and optimize energy efficiency in biomimetic models.

For smaller cone holes, such as the 2 mm case, the amount of "ingested soil" increases with increasing cone half-angle. This trend is evident in both measurements and simulations and implies that earthworms may adapt the cone angle formed by their heads during ingestion. By forming a wider tip, the earthworm facilitates a greater continuous inflow of soil into its mouth, enhancing energy intake. This behavior aligns with the observation that sharper tips tend to push soil aside, reducing intake, whereas blunter tips help channel soil into the digestive pathway. Again, these interpretations are based on mechanical analogues, and the actual intake by real earthworms may differ due to active suction and behavioral adaptations. Despite this

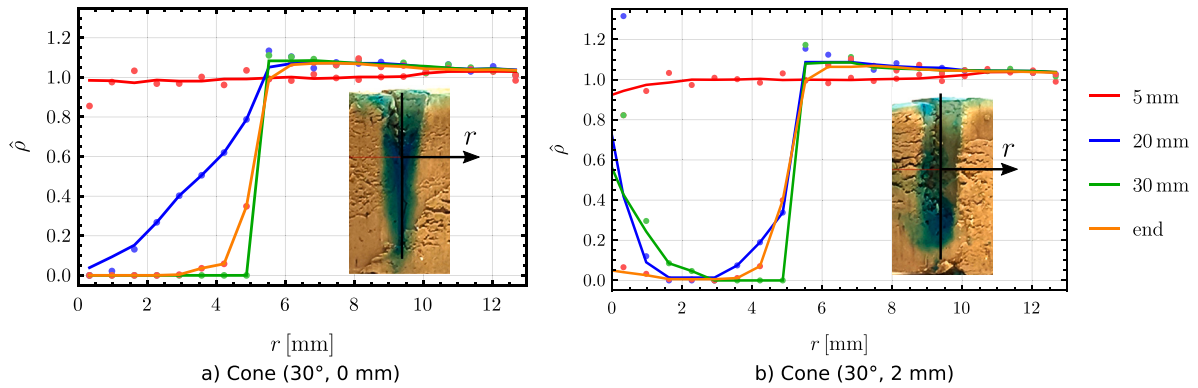

Fig. 9. The relative soil density $\hat{\rho}$ in the radial direction r in the DEM simulation in various time steps. The sampling size for the density calculation is $\Delta r = 0.65$ mm. The pictures show the soil profile after the measurement with the center line.

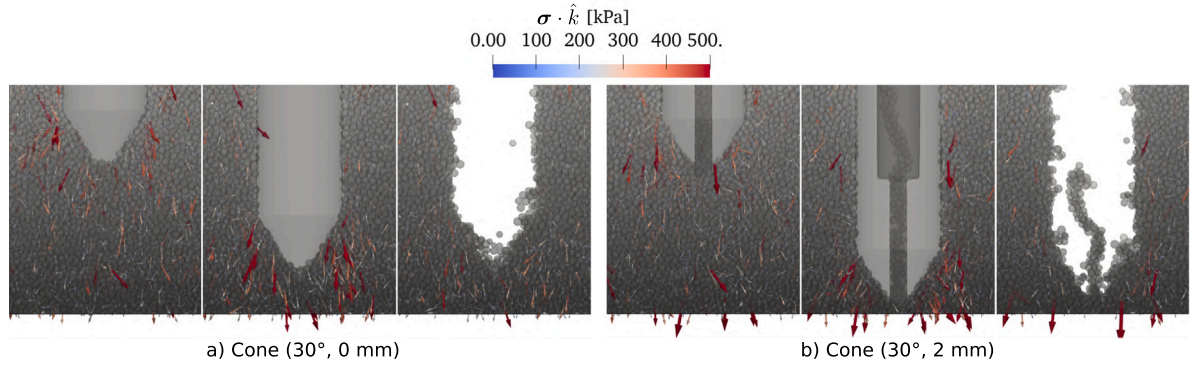

Fig. 10. Stress vectors in horizontal planes ($\boldsymbol{\sigma} \cdot \hat{k}$) in the DEM simulation in silt loam soil for two cones. The figures from left to right correspond to 20 mm penetration, 30 mm penetration and the soil state after penetration.

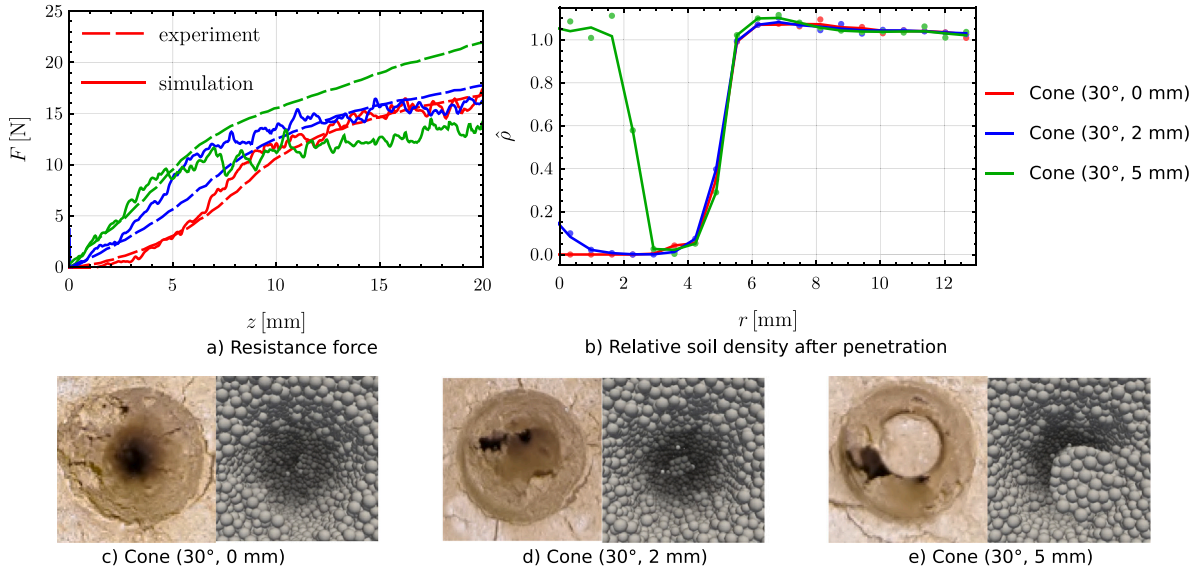

Fig. 11. The effect of hole size. (a) Resistance force F in the experiment (dashed lines) and DEM simulation (continuous lines) as a function of penetration depth z. (b) Relative soil density $\hat{\rho}$ in the radial direction r following the cone penetration. (c-e) Top view images of the burrows after the cones were removed in the experiments and simulations.

simplification, the combined experimental and DEM results provide a quantitative link between cone geometry and soil inflow, which was not previously captured.

The shape of the cone also strongly influences the resistance force. Sharper cones require smaller penetration forces, and the resulting compaction of the surrounding soil is less pronounced. This is consistent with the physical expectation that sharper tips more easily displace soil along a narrow path, whereas blunter tips compact more material laterally. These findings suggest that earthworms may optimize the tip sharpness dynamically, contracting longitudinal muscles to form a blunter tip when they need to ingest soil and using a sharper tip when the primary goal is cavity expansion. Both experiments and DEM

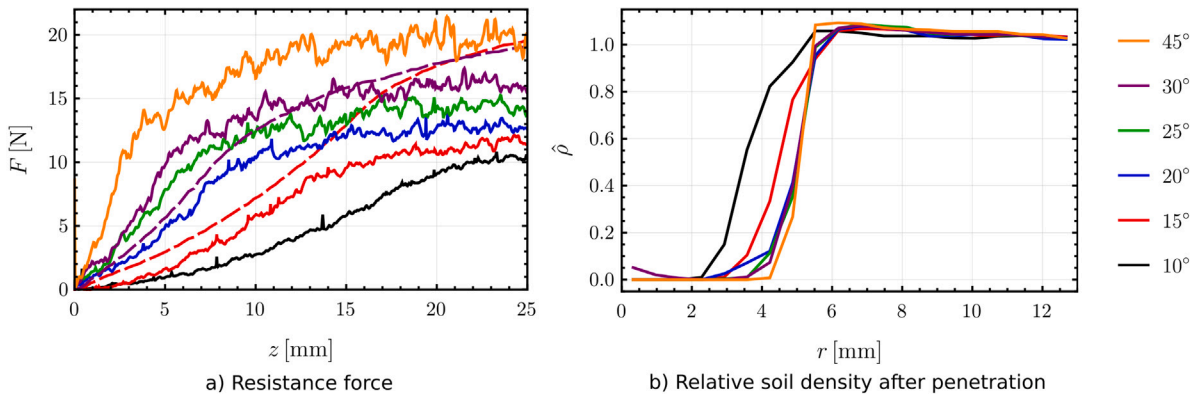

Fig. 12. The effect of the cone half-angle for a fixed 2 mm mouth diameter. For cone half-angles 15° and 30° measurement data is available and depicted with a dashed line in Panel (a).

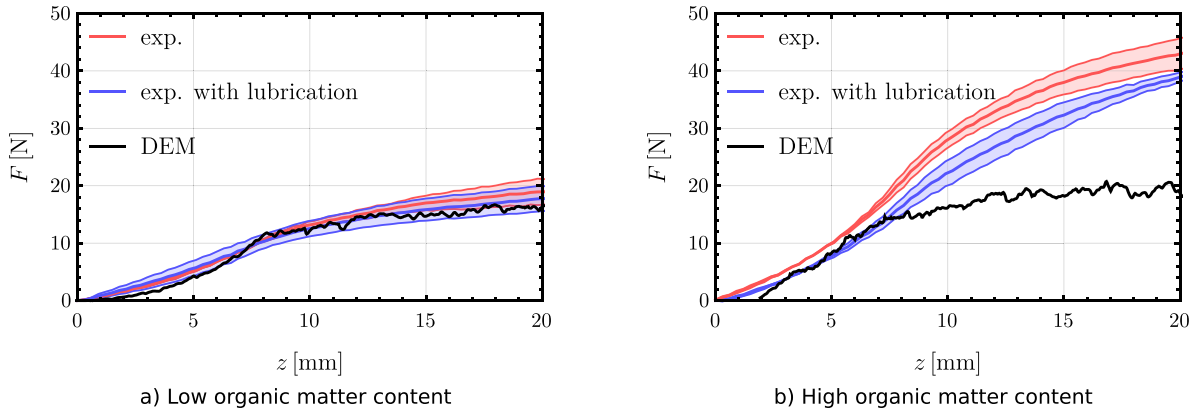

Fig. 13. Effect of lubrication on the penetration resistance F as a function of penetration depth z in (a) low and (b) high organic matter content silt loam soil for the (30°, 2 mm) cone. For the DEM simulations, only a single curve is shown, as variation of the cone wall friction did not affect the results. The regions around the red and blue curves depict the standard deviation of the measurements.

simulations show that a blunter tip requires more energy for burrowing but allows significantly more soil ingestion. Conversely, a sharper tip reduces the ingested soil but also lowers the required work. Results suggest that cone half-angles of 25°–30° are energetically optimal when considering the proportion of energy available for an earthworm from soil ingestion (input) and the required energy for burrowing (output). These energetic considerations represent a significant improvement over previous CPT studies mimicking earthworm penetration, as earlier work could not account for soil ingestion.

Our results show an increase in the penetration resistance in higher organic matter content soil. This increase is likely related to changes in soil cohesion, particle bonding, and organic binding agents, which interact with cone geometry in a non-trivial manner. Other potentially important parameters, such as soil water content, aggregate size distribution, and temperature, were not independently varied in our study. Previous studies indicate that increased moisture generally reduces penetration resistance (Ruiz et al., 2017), while smaller aggregate sizes tend to increase it (Ciantia et al., 2016). Furthermore, Whalen et al. (2004) suggested that temperature significantly influences the cast production of earthworms. These studies suggest that soil moisture, aggregate size and temperature may partially counteract the effects of soil organic matter. A systematic investigation of these coupled effects is left for future work to further refine the mechanistic interpretation of earthworm burrowing efficiency.

Finally, lubrication effects appear to be soil-dependent. In low organic content silt loam soil, lubrication has minimal influence on penetration force, although it slightly affects the amount of ingested soil measured in experiments. In contrast, in high organic content silt loam soil, lubrication reduces both the maximal force and the energy required for burrowing, likely by decreasing friction between particles and the cone surface; however, the current DEM model could not reproduce this, and further model development is necessary. In our study, we proposed a 0.4% agar solution as a proxy for earthworm mucus to investigate its effects. A more complex lubrication system could be developed that injects the lubricant along the cone shaft during penetration, an approach previously used in on-site geotechnical surveys (White, 2022). Our findings indicate that mucus secretion in earthworms may serve a functional role in more cohesive or sticky soils, but its effect on energy efficiency remains limited.

From a biological perspective, the main limitations of our study are the simplified representation of earthworm movement and soil ingestion. Natural burrowing paths are more complex and adaptive, but here a straight path was used for simplicity, as this is what can be achieved with traditional CPT. Similarly, soil ingestion was considered purely from a mechanistic perspective, without modeling active pharyngeal suction. A further limitation of the measurements is the relatively large variance in the results, which arises from the inhomogeneity of the soil and boundary effects despite the best efforts to prepare homogeneous soils. Consequently, the required penetration force varied significantly depending on the local soil conditions. A limitation of the DEM simulations is that they cannot accurately account for the effects of lubrication. Additionally, the simulated soil particles are larger than real soil grains, and the micromechanical parameters are selected based on model fitting rather than direct physical measurements. However, the two methods complement each other and help mitigate their respective weaknesses. The DEM simulations provide a more homogeneous

and controlled environment, making it easier to observe consistent trends, while the measurements serve to validate the simulations and confirm their physical relevance.

6. Conclusion

The present study demonstrated that the discrete element method, calibrated via a simple shear box test, can reliably reproduce cone penetration behavior in a silt loam soil using the fitted micromechanical parameters. The GPU-based calibration procedure proved both accurate and efficient, despite the large number of simulations required. Analysis of cone geometry revealed clear trends: more pointed cones reduce penetration resistance and induce smaller local soil compaction, while larger cone angles and hole diameters enhance soil ingestion and increase the energy available for burrowing. Our findings in a silt loam soil indicate that earthworms may achieve maximum energy efficiency by forming head cone half-angles of 25° – 30° given a 2 mm mouth diameter. Within this range, the available energy from soil ingestion is five-fold the energy requirement of burrowing. These results directly address the study objectives by linking cone geometry to both penetration resistance and soil ingestion, providing a quantitative framework to evaluate burrowing efficiency. Despite the simplifications regarding active soil ingestion and lubrication, the validated simulation framework offers a robust tool for future investigations into soil penetration, with potential applications in soil mechanics, biomimetics, and earthworm-inspired engineering.

CRediT authorship contribution statement

Kang Li: Writing – original draft, Methodology, Investigation, Formal analysis, Data curation, Conceptualization. **Dániel Nagy:** Writing – original draft, Visualization, Validation, Software, Methodology, Investigation, Formal analysis, Data curation, Conceptualization. **Thomas Keller:** Writing – review & editing, Supervision, Methodology, Conceptualization. **Kornél Tamás:** Writing – review & editing, Supervision, Resources, Project administration, Methodology, Investigation, Funding acquisition, Formal analysis, Conceptualization.

Declaration of competing interest

The authors declare that they have no known competing financial interests or personal relationships that could have appeared to influence the work reported in this paper.

Acknowledgments

We thank Zoltán Huboda from the Department of Machine and Product Design, Budapest University of Technology and Economics for his guidance. We thank Zoltán Tompai, Ferenc Némethy and Norbert Némethy from the Geotechnics and Engineering Geology Laboratory, Budapest University of Technology and Economics, for their guidance and for providing the experimental equipment. We also thank Daniel Iseskog from the Soil Mechanics and Soil Management Laboratory, Swedish University of Agricultural Sciences, Uppsala for manufacturing the steel cones. The work of Kang Li was supported by the dr. ir. Aalt Dijkhuizen Fund in the Wageningen University. This paper was supported by the Hungarian Scientific Research Fund, Hungary (NKFIH FK-146067). Project No. 2025-2.1.2-EKÖP-KDP-2025-00005 has been implemented with the support provided by the Ministry of Culture and Innovation of Hungary, from the National Research, Development and Innovation Fund, financed under the EKÖP_KDP-25-1-BME-6 funding scheme. Thomas Keller acknowledges funding from the Swedish Research Council for Sustainable Development (Formas), grant no 2021-00966. Project no. TKP-9-8/PALY-2021 has been implemented with the support provided by the Ministry of Culture and Innovation of Hungary from the National Research, Development and Innovation Fund, financed under the TKP2021-EGA funding scheme.

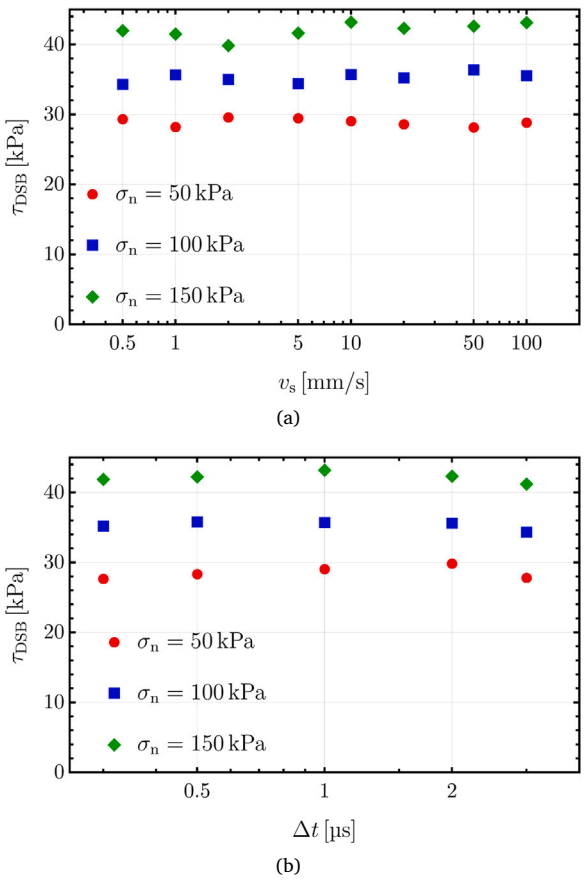

Fig. A.14. Effect of (a) shear velocity v_s and (b) time step size Δt on the shear stress τ_{DSB} measured in the shear box test using DEM for three load cases.

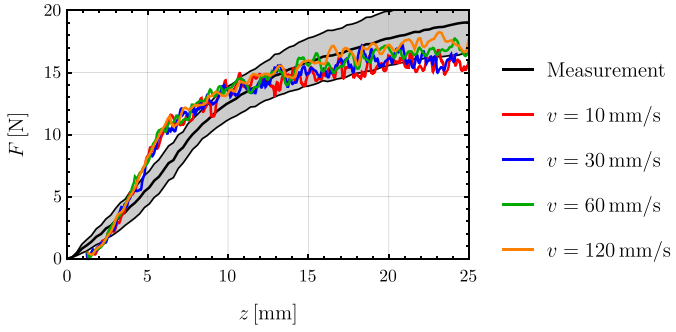

Fig. B.15. Penetration resistance F as function of the penetration depth z for various penetration velocities v in the DEM simulation of the CPT. The gray region represents the standard deviation of the repeated measurements.

Appendix A. Effect of time step and shear velocity in DSB

The influence of time step size and shear velocity on the resulting shear stress was investigated. As shown in Fig. A.14, within the range of $v_s = 0.5 \ldots 100$ m/s and $\Delta t = 0.2 \ldots 2$ µs, the specific choice of shear velocity and time step size did not significantly affect the computed shear stress. This indicates that the results are physically meaningful and not influenced by these simulation parameters.

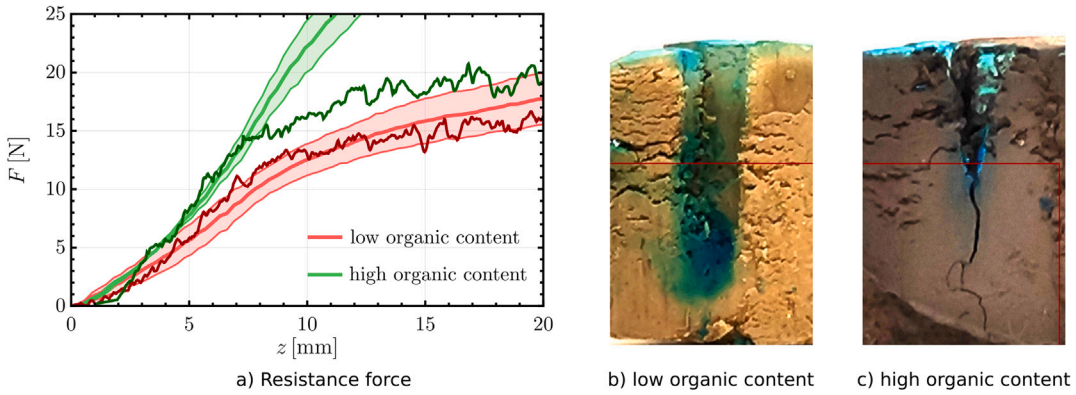

Fig. C.16. The effect of organic matter content in silt loam soil. (a) Resistance force in the measurements (light regions) and in the DEM simulation (darker lines). (b-c) Soil profiles in the measurement after penetration.

Appendix B. Effect of penetration velocity in DSB

The influence of penetration velocity was investigated in the DEM simulation of the CPT. Fig. B.15 shows the resistance force as a function of displacement for various penetration velocities, as indicated in the legend. These results show that penetration velocity does not significantly affect the required penetration force; therefore, using a velocity higher than the real experimental value is justified. For this study, a velocity of $10\,\mathrm{mm/s}$ was applied.

Appendix C. High organic matter content silt soil

Simulations and experiments were carried out in high organic content silt loam soil using cone (30°, 2 mm). For the high organic content silt loam soil, the best agreement with the measured penetration force was achieved for the most compacted soil state, corresponding to porosity of 23%.

Fig. C.16a shows the penetration resistance as a function of penetration depth in the two different silt loam soils for cone ($30°, 2\,\mathrm{mm}$). The shaded regions in the background represent experimental measurements with the standard deviation, while the darker lines indicate the results of the DEM simulations. The agreement between simulation and experiment is good for the low organic content silt loam soil. However, for the high organic content silt loam soil, only the initial phase of penetration matches the experimental data. The maximum penetration force stabilizes around $20\,\mathrm{N}$ in the simulation in that case. This discrepancy can be attributed to limitations in the shear box parameter calibration and the DEM model only using spherical particles. For the high organic content soil, the DEM model was unable to reproduce the nonlinear relationship between the required shear force and the applied normal load. As penetration depth increases, a larger volume of soil undergoes shearing, amplifying the mismatch between simulation and experiment.

The soil profiles after the cone penetration experiments are shown in Fig. C.16b-c. The low organic content soil appears visibly more porous, while high organic content soil exhibit fewer radial cracks and seem more homogeneous, especially near the bottom. This observation aligns with the DEM results: the best fit for penetration resistance in the high organic content soils is achieved under maximum compaction, whereas only moderate compaction is required for the low organic content soil. In the experiments, lubrication slightly reduced the resistance in the high organic content soil. Specifically, the average energy required for penetration decreased by 11% for the high organic content silt loam soil.

Data availability

Data will be made available on request.

References

Abchiche, H., Mellal, M., Sahraoui, N., Bertouche, S., Tebachi, L., Mameri, A., 2020. The study of the effect of concentration of the Agar-Agar solution on the rheological and thermo rheological behavior. Eur. J. Eng. Sci. Tech. 3, 1–9. http://dx.doi.org/10.33422/ejest.v3i1.166.

Arrazola-Vasquez, E.M., Larsbo, M., Capowiez, Y., Taylor, A., Herrmann, A.M., Keller, T., 2024. Estimating energy costs of earthworm burrowing using calorimetry. Eur. J. Soil Biol. 121, 103619. http://dx.doi.org/10.1016/j.ejsobi.2024.103619.

Arrázola-Vásquez, E., Larsbo, M., Capowiez, Y., Taylor, A., Sandin, M., Iseskog, D., Keller, T., 2022. Earthworm burrowing modes and rates depend on earthworm species and soil mechanical resistance. Appl. Soil Ecol. 178, 104568. http://dx.doi.org/10.1016/j.apsoil.2022.104568.

ASTM, 2019. Standard test methods for laboratory determination of water (moisture) content of soil and rock by mass. ASTM, http://dx.doi.org/10.1520/D2216-19.

ASTM, 2021. Standard Test Method for California Bearing Ratio (CBR) of Laboratory-Compacted Soils. ASTM, http://dx.doi.org/10.1520/D1883-21.

Asyakina, L., Dyshlyuk, L., 2016. Study of viscosity of aqueous solutions of natural polysaccharides. Sci. Evol. 1 (2), 11–19.

Bahrami, M., Naderi-Boldaji, M., Ghanbarian, D., Ucgul, M., Keller, T., 2020. Simulation of plate sinkage in soil using discrete element modelling: Calibration of model parameters and experimental validation. Soil Tillage Res. 203, 104700. http://dx.doi.org/10.1016/j.still.2020.104700.

Barbosa, L.A.P., Gerke, H.H., 2023. Continuum and discrete element modelling for describing coupled hydro-mechanical effects of earthworm burrow coatings on soil shrinkage. Geoderma 435, 116497. http://dx.doi.org/10.1016/j.geoderma.2023.116497.

Bernhardt, M.L., Biscontin, G., et al., 2016. Experimental validation study of 3D direct simple shear dem simulations. Soils Found. 56 (3), 336–347. http://dx.doi.org/10.1016/j.sandf.2016.04.002.

Bolton, P., Phillipson, J., 1976. Burrowing, feeding, egestion and energy budgets of allolobophora rosea (savigny)(lumbricidae). Oecologia 23 (3), 225–245. http://dx.doi.org/10.1007/BF00361238.

Chen, Y., Martinez, A., DeJong, J., 2022. DEM study of the alteration of the stress state in granular media around a bio-inspired probe. Can. Geotech. J. 59 (10), 1691–1711. http://dx.doi.org/10.1139/cgj-2021-0260.

Ciantia, M.O., Arroyo, M., Butlanska, J., Gens, A., 2016. DEM modelling of cone penetration tests in a double-porosity crushable granular material. Comp. Geotech. 73, 109–127. http://dx.doi.org/10.1016/j.compgeo.2015.12.001.

Coetzee, C.J., 2017. Calibration of the discrete element method. Powder Technol. 310, 104–142. http://dx.doi.org/10.1016/j.powtec.2017.01.015.

Cortes, D., John, S., 2018. Earthworm-inspired soil penetration. In: Proc. of Biomediated and Bioinspired Geotech. (B2G) Conf..

Cui, J., Xie, L., Wang, J., Zhu, L., Qin, Y., 2023. Influence of particle gradation and penetration velocity on deformation behavior of sandy soil based on CPT. Geotech. Geol. Eng. 41 (6), 3663–3680. http://dx.doi.org/10.1007/s10706-023-02480-y.

Cundall, P.A., 1979. A discrete numerical model for granular assemblies. Geotechnique 29, 47–65. http://dx.doi.org/10.1680/geot.1979.29.1.47.

Curry, J.P., Schmidt, O., 2007. The feeding ecology of earthworms–a review. Pedobiologia 50 (6), 463–477. http://dx.doi.org/10.1016/j.pedobi.2006.09.001.

Dhaouadi, W., Marteau, E., Kolvenbach, H., Choukroun, M., Molaro, J.L., Hodyss, R., Schulson, E.M., 2022. Discrete element modeling of planetary ice analogs: mechanical behavior upon sintering. Granul. Matter 24, 1–20. http://dx.doi.org/10.1007/s10035-021-01167-6.

Dong, Y., Yan, D., Cui, L., 2022. An efficient parallel framework for the discrete element method using GPU. Appl. Sci. 12 (6), 3107. http://dx.doi.org/10.3390/app12063107.

Ducasse, V., Darboux, F., Auclerc, A., Legout, A., Ranger, J., Capowiez, Y., 2021. Can lumbricus terrestris be released in forest soils degraded by compaction? Preliminary results from laboratory and field experiments. Appl. Soil Ecol. 168, 104131. http://dx.doi.org/10.1016/j.apsoil.2021.104131.

Edwards, C.A., Bohlen, P.J., Hendrix, P., Arancon, N., 1996. Biology and ecology of earthworms, vol. 3, Springer.

Gajalakshmi, S., Abbasi, S., 2004. Earthworms and vermicomposting. CSIR.

Ghali, M., Chekired, M., Karray, M., 2019. A laboratory-based study correlating cone penetration test resistance to the physical parameters of uncemented sand mixtures and granular soils. Eng. Geol. 255, 11–25.

Golshan, S., Munch, P., Gassmöller, R., Kronbichler, M., Blais, B., 2023. Lethe-DEM: An open-source parallel discrete element solver with load balancing. Comp. Part. Mech. 10 (1), 77–96. http://dx.doi.org/10.1007/s40571-022-00478-6.

Guo, N., Liu, H., Li, B., Yang, Z., 2023. DEM study of the stress fields around the closed-ended displacement pile driven in sand. Can. Geotech. J. 61 (3), 549–561. http://dx.doi.org/10.1139/cgj-2023-0025.

Head, K.H., Epps, R., 1980. Manual of soil laboratory testing, vol. 1, (2), Pentech press London.

Horváth, D., Tamás, K., Poós, T., 2022. Viscoelastic contact model development for the discrete element simulations of mixing process in agitated drum. Powder Technol. 397, 117038. http://dx.doi.org/10.1016/j.powtec.2021.117038.

ISO, S.T.E., 2019. 17892-10. Geotechnical investigation and testing—Laboratory testing of soil—Part 10: Direct shear tests. SIST: Ljubl. Slov..

Israelachvili, J.N., 2011. Intermolecular and surface forces. Academic Press.

Jiang, M., Dai, Y., Cui, L., Shen, Z., Wang, X., 2014. Investigating mechanism of inclined CPT in granular ground using DEM. Granul. Matter 16, 785–796. http://dx.doi.org/10.1007/s10035-014-0508-2.

Johnson, K.L., Kendall, K., Roberts, A., 1971. Surface energy and the contact of elastic solids. Proc. R. Soc. A 324 (1558), 301–313. http://dx.doi.org/10.1098/rspa.1971.0141.

Kasteel, R., Burkhardt, M., Giesa, S., Vereecken, H., 2005. Characterization of field tracer transport using high-resolution images. Vadose Z. J. 4 (1), 101–111. http://dx.doi.org/10.2113/4.1.101.

Keppler, I., Safranyik, F., Oldal, I., 2016. Shear test as calibration experiment for DEM simulations: a sensitivity study. Engi. Comp. 33 (3), http://dx.doi.org/10.1108/EC-03-2015-0056.

Khosravi, A., Martinez, A., DeJong, J., 2020. Discrete element model (DEM) simulations of cone penetration test (CPT) measurements and soil classification. Can. Geotech. J. 57 (9), 1369–1387. http://dx.doi.org/10.1139/cgj-2019-0512.

Kosaku, Y., Tsunazawa, Y., Tokoro, C., 2023. A coarse grain model with parameter scaling of adhesion forces from liquid bridge forces and JKR theory in the discrete element method. Chem. Eng. Sci. 268, 118428. http://dx.doi.org/10.1016/j.ces.2022.118428.

Mao, N., Li, X., Wei, X., Shao, M., 2024. The effects of roots and earthworms on aggregate size distribution and their associated carbon under contrasting soil types and soil moisture conditions. Catena 246, 108434. http://dx.doi.org/10.1016/j.catena.2024.108434.

Marshall, J.S., 2009. Discrete-element modeling of particulate aerosol flows. J. Comput. Phys. 228 (5), 1541–1561. http://dx.doi.org/10.1016/j.jcp.2008.10.035.

Martin, A., Mariotti, A., Balesdent, J., Lavelle, P., 1992. Soil organic matter assimilation by a geophagous tropical earthworm based on (delta)ˆ(13) c measurements. Ecology 73 (1), 118–128. http://dx.doi.org/10.2307/1938725.

Mishra, A.K., Tramacere, F., Guarino, R., Pugno, N.M., Mazzolai, B., 2018. A study on plant root apex morphology as a model for soft robots moving in soil. PLoS One 13 (6), e0197411. http://dx.doi.org/10.1371/journal.pone.0197411.

Nagy, D., Pásthy, L., Tamás, K., 2024. Development of a GPU-based DEM solver for parameter optimization in the simulations of soil-sweep tool interactions. Comput. Electron. Agric. 227, 109482. http://dx.doi.org/10.1016/j.biosystemseng.2018.02.001.

Nitka, M., Grabowski, A., 2021. Shear band evolution phenomena in direct shear test modelled with DEM. Powder Technol. 391, 369–384. http://dx.doi.org/10.1016/j.powtec.2021.06.025.

Pribyl, D.W., 2010. A critical review of the conventional SOC to SOM conversion factor. Geoderma 156 (3–4), 75–83. http://dx.doi.org/10.1016/j.geoderma.2010.02.003.

Pásthy, L., Graeff, J., Tamás, K., 2022. Development of a 2D discrete element software with labview for contact model improvement and educational purposes.. In: ECMS. pp. 203–209.

Randolph, M., May, M., Leong, E., Hyden, A., Murff, J., 1992. Soil plug response in open-ended pipe piles. J. Geotech. Eng. 118 (5), 743–759. http://dx.doi.org/10.1061/(ASCE)0733-9410(1992)118:5(743).

Ruiz, S.A., 2018. Mechanics and energetics of soil bioturbation by earthworms and growing plant roots (Ph.D. thesis). ETH Zurich.

Ruiz, S., Schymanski, S.J., Or, D., 2017. Mechanics and energetics of soil penetration by earthworms and plant roots: Higher rates cost more. Vadose Z. J. 16 (8), 1–16. http://dx.doi.org/10.2136/vzj2017.01.0021.

Ruiz, S., Straub, I., Schymanski, S.J., Or, D., 2016. Experimental evaluation of earthworm and plant root soil penetration–cavity expansion models using cone penetrometer analogs. Vadose Zone J. 15 (3), vzj2015–09.

Sinnett, D., Morgan, G., Williams, M., Hutchings, T., 2008. Soil penetration resistance and tree root development. Soil Use Manag. 24 (3), 273–280. http://dx.doi.org/10.1111/j.1475-2743.2008.00164.x.

Soil Survey Staff, 2014. Kellogg soil survey laboratory methods manual. Soil Surv. Investig. Rep. No. 42, Version 5.0.

Solutions, D., 2014. EDEM 2.6 theory reference guide. Edinb. United Kingd..

Tamás, K., 2018. The role of bond and damping in the discrete element model of soil-sweep interaction. Biosyst. Eng. 169, 57–70. http://dx.doi.org/10.1016/j.biosystemseng.2018.02.001.

Tsuji, Y., Tanaka, T., Ishida, T., 1992. Lagrangian numerical simulation of plug flow of cohesionless particles in a horizontal pipe. Powder Technol. 71 (3), 239–250. http://dx.doi.org/10.1016/0032-5910(992)88030-L.

Uteau, D., Horn, R., Peth, S., 2022. Millimetre scale aeration of the rhizosphere and drilosphere. Euro. J. Soil Sci. 73 (4), e13269. http://dx.doi.org/10.1111/ejss.13269.

Vidal, A., Blouin, M., Lubbers, I., Capowiez, Y., Sanchez-Hernandez, J.C., Calogiuri, T., van Groenigen, J.W., 2023. The role of earthworms in agronomy: Consensus, novel insights and remaining challenges. Adv. Agron. 181, 1–78. http://dx.doi.org/10.1016/bs.agron.2023.05.001.

Whalen, J.K., Sampedro, L., Waheed, T., 2004. Quantifying surface and subsurface cast production by earthworms under controlled laboratory conditions. Biology Fertil. Soils 39 (4), 287–291.

White, D., 2022. CPT equipment: Recent advances and future perspectives. Cone Penetration Test. 2022 66–80.

Yu, Z., Zhan, J., Wang, H., Zheng, H., Xie, J., Wang, X., 2020. Analysis of influencing factors on viscosity of agar solution for capsules. In: Journal of Physics: Conference Series, vol. 1653, (1), IOP Publishing, 012059. http://dx.doi.org/10.1088/1742-6596/1653/1/012059.

Zeraati-Shamsabadi, M., Sadrekarimi, A., 2025. A DEM study on the effects of specimen and particle sizes on direct simple shear tests. Granul. Matter 27 (2), 36. http://dx.doi.org/10.1007/s10035-025-01513-y.

Zhang, D., Chen, Y., Ma, Y., Guo, L., Sun, J., Tong, J., 2016. Earthworm epidermal mucus: Rheological behavior reveals drag-reducing characteristics in soil. Soil Till. Res. 158, 57–66. http://dx.doi.org/10.1016/j.still.2015.12.001.

Zhang, J., Wen, N., Sun, Q., Horton, R., Liu, G., 2023. The effect of macropore morphology of actual anecic earthworm burrows on water infiltration: A COMSOL simulation. J. Hydrol. 618, 129261. http://dx.doi.org/10.1016/j.jhydrol.2023.129261.